Polarimetric SAR Image Filtering by Infinite Number of Looks Prediction Technique

Mohamed Yahia ⓘ, Tarig Ali ⓘ, *Senior Member, IEEE*, Md. Maruf Mortula ⓘ, Riadh Abdelfattah, *Senior Member, IEEE*, and Samy Elmahdy

Abstract—Speckle filtering in synthetic aperture radar (SAR) and polarimetric SAR (PolSAR) images is indispensable before the extraction of the useful information. The minimum mean square error estimate of the filtered pixels conducted to the definition of a linear rule between the values of the filtered pixels and their variances. Hence, the filtered pixel for infinite number of looks (INL) is predicted by a linear regression of means and variances for various window sizes. In this article, the infinite number of looks prediction (INLP) filter is explored in details to emphasize its ability to reduce speckle and preserve the spatial details. Then, the linear regression rule has been adapted to PolSAR context in order to preserve the polarimetric information. The number of the processed pixels used in the linear regression is adjusted to the variability of the scene. This effort increased the filtering performances. The reduction of the correlation between the pixels which constitutes an additional filtering criterion is discussed. Compared to the initially applied filter, the results showed that the improved INLP filter increased in speckle reduction level, augmented the preservation of the spatial details, increased the spatial resolution, reduced the correlation between the pixels and better preserved the polarimetric information. Simulated, one-look and multilook real PolSAR data were used for validation.

Index Terms—Linear regression, minimum mean square error (MMSE) filter, polarimetric synthetic aperture radar (PoLSAR), speckle filtering.

I. INTRODUCTION

REMOTE sensing imagery represents nowadays an important source of information for the analysis of the Earth's surface. The potentiality of synthetic aperture radar (SAR)

Mohamed Yahia is with the GIS and Mapping Laboratory, American University of Sharjah, Sharjah 26666, United Arab Emirates, and also with the Laboratoire de Recherche Modélisation Analyse et Commande de Systèmes-MACS, Ecole Nationale d'Ingénieurs de Gabes, Université de Gabes, Tunisia 6029, Tunisia (e-mail: mohamed_yahia1@yahoo.fr).

Tarig Ali and Samy Elmahdy are with the GIS and Mapping Laboratory, American University of Sharjah, Sharjah 26666, United Arab Emirates (e-mail: atarig@aus.edu; selmahdy@aus.edu).

Md. Maruf Mortula is with the Department of Civil Engineering, American University of Sharjah, Sharjah 26666, United Arab Emirates (e-mail: mmortula@aus.edu).

Riadh Abdelfattah is with the COSIM Laboratory, Higher School of Communications of Tunis, University of Carthage, Ariana 2083, Tunisia, and also with the Department of ITI, Télécom Bretagne, Institut de Télécom, 29238 Brest, France (e-mail: riadh.abdelfattah@supcom.tn).

Digital Object Identifier 10.1109/JSTARS.2021.3070421

and polarimetric SAR (PoSAR) systems are recognized for geoscience and remote sensing applications due to their operation in all weather and all-time conditions. However, SAR data are affected by the speckle noise, caused by the coherent nature of the scattering mechanisms [1]. The presence of speckle noise affects human interpretation of the images as well as the accuracy of postprocessing, such as image classification [2].

Several PolSAR have been proposed in the literature to overcome this problem. Based on the multiplicative-additive speckle noise model [3], the model-based PolSAR filter [4] is proposed. The intensity-driven adaptive-neighborhood filter used a region growing technique to produce an adaptive homogeneous neighborhood [5]. The nonlocal nonlocal (NL) filtering represents one of the powerful speckle reduction techniques. These filtering techniques include the pretest filter [6], the stochastic based filter [7], the NL-SAR filter [8], the NL-discriminative similarity measure NL-DSM filter [9], the NL-distributed Lee filter [10]. The mean shift filter (MSF), which is commonly used in filtering, segmentation, clustering, and object tracking in the field of pattern recognition, has been generalized in PolSAR filtering [11]. Total variation (TV) constitutes another trend for PolSAR speckle filtering [12]–[14]. Deep Learning techniques have been newly proposed for PolSAR image filtering [15]–[17]. The iterative minimum mean square error (MMSE) filtering showed promising results in both SAR [18] and PolSAR filtering [19].

The MMSE-based filters have been widely applied in PolSAR speckle filtering. Lee *et al.* [20] proposed a technique to reduce speckle in multipolarization images. Goze and Lopes [21] extended this approach to filter the entire covariance matrix. Touzi *et al.* extended this technique to filter the Mueller matrix [22]. However, the last techniques did not preserve the polarimetric information [2]. To tackle this problem, Lee et al. established some fundamental constraints of PolSAR speckle filtering [2]. After that, most of MMSE-based PoLSAR filters have has mainly focused on the selection of pixels having similar scattering properties. In [2], the most homogeneous window is selected from eight edge aligned windows. In [23], the scattering model-based method selects pixels of the same scattering mechanisms to be included in the filtering. In [24], the homogeneous pixels are selected from the sigma range. In [25], the homogeneous pixels are selected using the scattering mechanism and the intensity information. In [26], the shape and size of the window filter is adapted using a homogeneity measurement. Nevertheless,

all cited filters exploited the statistics of the original speckled image only.

In [27], a linear regression of means and variances of the sample eigenvalues for different window sizes is applied to estimate the true eigenvalues. Results showed that this technique compensated the biases and reduced the noise of the eigenvalues. Based on the analogies between the eigenvalues and the intensity channels of PolSAR data, an infinite number of looks prediction (INLP) technique has been applied to improve the filtering performance of SAR images [28]. In [29], the INLP filter is adapted to PolSAR filtering. In this article, a theoretical effort has been made to demonstrate the effectiveness of the INLP filter. Its impacts in the speckle reduction, correlation between the pixels, spatial detail preservation, computational complexity (CP) and polarimetric information preservation is investigated.

The rest of this article is organized as follows: Section II introduces SAR polarimetry. In Section III, the INLP technique is introduced. Section IV presents results obtained using PolSAR images. Finally, Section V gives the conclusions of this article.

II. Improved INLP Filter

The multiplicative noise model of SAR images is [1]

$$y(i,j) = x(i,j)\,\nu(i,j) \tag{1}$$

ν is the speckle having unit mean and standard deviation σ_v and x is the noise free pixel. For clarity, the (i,j) index is removed. The MMSE-based filtered pixel $\hat{x}$ is [1], [2], [18]–[19]

$$\hat{x} = \bar{y} + d\,(\mathrm{var}(y))\,(y - \bar{y}) \tag{2}$$

where

$$d\,(\mathrm{var}(y)) = \frac{\mathrm{var}(x)}{\mathrm{var}(y)} \tag{3}$$

and

$$\mathrm{var}(x) = \frac{\mathrm{var}(y) - \bar{y}^2 \sigma_v^2}{(1 + \sigma_v^2)} \tag{4}$$

then

$$d\,(\mathrm{var}(y)) = \frac{\mathrm{var}(y) - \bar{y}^2 \sigma_v^2}{(1 + \sigma_v^2)\mathrm{var}(y)}. \tag{5}$$

Equations (2) and (3), give

$$\bar{\hat{x}} = \overline{\bar{y} + \frac{\mathrm{var}(x)}{\mathrm{var}(y)}\,(y - \bar{y})} = \bar{y} = x \tag{6}$$

$$\mathrm{var}(\widehat{x}) = E\left(\left(\left(\bar{y} + \frac{\mathrm{var}(x)}{\mathrm{var}(y)}\,(y - \bar{y})\right) - \bar{y}\right)^2\right)$$
$$= \left(\frac{\mathrm{var}(x)}{\mathrm{var}(y)}\right)^2 E\,(y - \bar{y})^2 \tag{7}$$

$$\mathrm{var}(\widehat{x}) = \left(\frac{\mathrm{var}(x)}{\mathrm{var}(y)}\right)\mathrm{var}(x) = d\mathrm{var}(x) \tag{8}$$

then,

$$\hat{x} = x + \frac{(y - x)}{\mathrm{var}(x)}\mathrm{var}(\hat{x}). \tag{9}$$

This equation can be written as

$$\hat{x} = a\,\mathrm{var}(\hat{x}) + b \tag{10}$$

where

$$a = (y - x)/\mathrm{var}(x) \tag{11}$$

and

$$b = x. \tag{12}$$

Equation (10) demonstrated that the filtered pixel $\hat{x}$ is a linearly related to its variance $\mathrm{var}(\hat{x})$. This linearity is exploited to compute the INLP filtered pixel (i. e. the parameter b) [28]. In (10), $\hat{x}$ is the filtered pixel given by (2), b is INLP filtered pixel and (a $\mathrm{var}(\hat{x})$) is the difference between both values.

A. Improved Formulation

In the INLP filtering, the coefficients a and b of (10) are approximated by a linear regression. To demonstrate the usefulness of the INLP filter, the linear regression theory is reviewed. Let U and V be two random vectors representing $\hat{X} = (\hat{x} \quad \hat{x}_{N-1} \quad \ldots)$ and $\mathrm{var}\hat{X} = (\mathrm{var}\hat{x}_N \quad \mathrm{var}\hat{x}_{N-1} \quad \ldots)$ respectively. The linearity between U and V can be approximated by the following linear regression:

$$U_i = a'V_i + b'. \tag{13}$$

The coefficients a' and b' represent the MMSE estimation (i. e. linear regression) of the coefficients a and b where [30]

$$b' = \bar{U} - a'\bar{V} \tag{14}$$

and

$$a' = -\frac{\overline{UV} - \bar{U}\bar{V}}{\overline{V^2} - \bar{V}^2} = \frac{\bar{U}\bar{V} - \overline{UV}}{\mathrm{var}(V)} \tag{15}$$

Then

$$b' = \bar{U} + \frac{\overline{UV} - \bar{U}\bar{V}}{\overline{V^2} - \bar{V}^2}\bar{V} = \bar{U} + \frac{\bar{V}}{\overline{V^2} - \bar{V}^2}\left(\overline{UV} - \bar{U}\bar{V}\right) \tag{16}$$

$$b' = \bar{U} + \frac{\bar{V}}{\overline{V^2} - \bar{V}^2}\frac{1}{M}\left(\sum_{i=1}^{M} V_i\,(U_i - \bar{U})\right). \tag{17}$$

Finally

$$b' = \bar{U} + g(V)\left(U - \bar{U}\right)^t \tag{18}$$

where

$$g(V_i) == \frac{\bar{V}}{\overline{V^2} - \bar{V}^2}\frac{V_i}{M}, \; i = 1 \ldots M. \tag{19}$$

It can be observed from (2) that $\hat{x}$ is a combination of y and $\bar{y}$ pondered by the function d which depends on the variance $\mathrm{var}(y)$. By analogy, the parameter b' (18) is a combination of U_i and $\bar{U}$ pondered by the function g which depends on the variance V_i. Again, the objective is to demonstrate that (18) outperforms (2) in spatial detail preservation as in speckle reduction. For $M = 1$, (18) and (2) are equivalent.

As stated previously, all filtered pixels $\hat{x}_i$ for different window sizes ($i=N, N-1, \ldots N_{\min}$) verify (9) and (10). As a result

$$\hat{x}_N = x + \frac{(y-x)}{\text{var}(x)}\text{var}(\hat{x}_N) \qquad (20)$$

$$\hat{x}_{N-1} = x + \frac{(y-x)}{\text{var}(x)}\text{var}(\hat{x}_{N-1}) \qquad (21)$$

$$\vdots$$

$$\hat{x}_{N\min} = x + \frac{(y-x)}{\text{var}(x)}\text{var}(\hat{x}_{N\min}). \qquad (22)$$

By averaging $\hat{x}_i$, we obtain

$$\bar{\hat{x}} = x + \frac{(y-x)}{\text{var}(x)}\overline{\text{var}(\hat{x})} = b + a\,\overline{\text{var}(\hat{x})}. \qquad (23)$$

Finally

$$b = \bar{U} - a\,\bar{V}. \qquad (24)$$

Hence, the MMSE estimation (24) is analog to the linear regression (14) where the parameter *a'* constitutes the MMSE estimation of the parameter. Nevertheless, the MMSE estimation (24) cannot be applied to compute *b* since the parameter *a* is unknown. This limitation is surmounted by applying the linear regression where the parameter *a'* can be estimated from the available data. In the rest of the article, the parameter *b'* represents the INLP filtered pixel.

The objective of this study is to demonstrate that the INLP filtering [i.e., (18)] outperforms the classical spatial filtering [i.e., (2)].

B. Speckle Reduction

From (1), we have $x = \bar{y}$ i.e.. the mean of the infinite homogeneous samples. This value is usually approximated by the use of small homogeneous samples. Let consider a homogeneous area containing *N* homogeneous independent pixels. In (2), *d* = 0, and $\hat{x} = \bar{y}$ (i. e. *N*-looking). On the other hand, in the INLP filter, the noise free pixel is $x = b'$ ($b' = \bar{y}$ for infinite samples see (18)). For finite samples (i. e. *N* homogeneous samples), $b' \neq \bar{y}$. A question arises: Which parameter ensured better speckle reduction level? *b'* (18) or $\bar{y}$ (2).

Let assume having infinite homogeneous pixels. The filtered pixels $\hat{x}$ (2) for *N, N-1, N-2,..* -looks can be obtained. The variances of the filtered pixels are

$$\text{var}(\hat{x}_N) = x^2/N. \qquad (25)$$

Fig. 1(a) displays the scatter plots of the filtered pixels for various window sizes. The variances of the filtered pixels decrease with the respect increase of the averaging samples. When averaging infinite pixels $\text{var}(\hat{x}_\infty) = 0$ and $\hat{x}_\infty = x$. However, in real data, the number of homogeneous pixels is finite (i.e., *N* pixels). In classical spatial speckle filters, the optimal scenario is to average the *N* pixels. The equivalent number of looks obtained is *N*. In the INLP filter, contrarily to classical spatial filtering
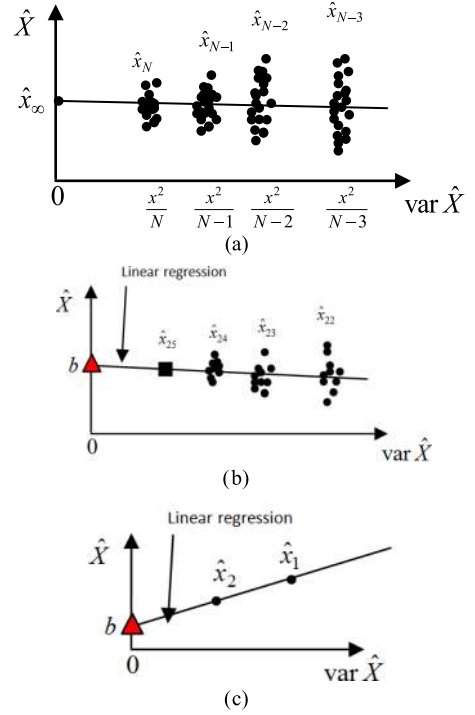

Fig. 1. (a) Scatter plots of the filtered pixels of an homogeneous area for various window sizes. (b) INLP filter ($N = 25$, L=10, $N_{\min} = 22$). c) INLP using 2 samples ($b < \hat{x}_2$).
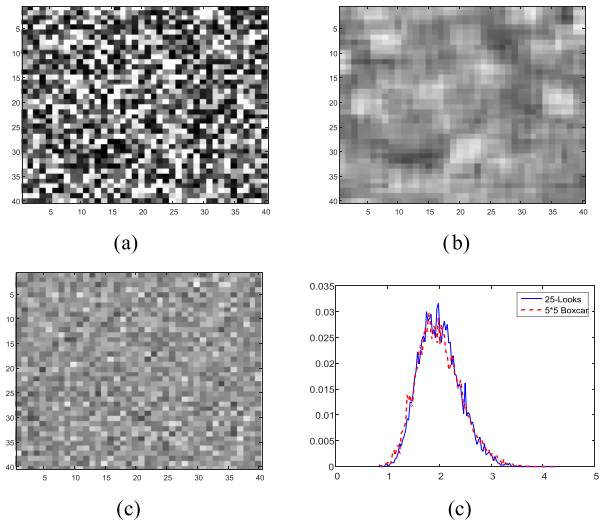

Fig. 2. (a) Speckled image. (b) 5×5 boxcar. (c) 25-looks (averaging 25 independent images). (d) Pdfs 5×5 boxcar and 25-looks.
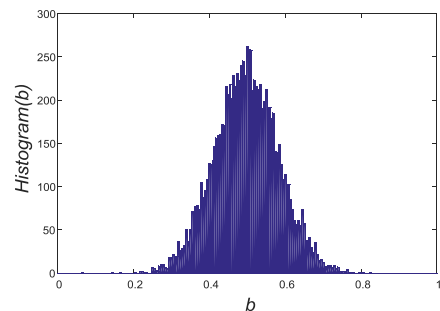

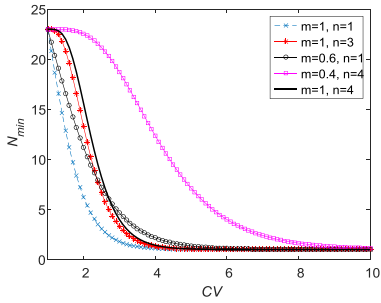Fig. 3. Histogram of the parameter *b'* (14).

Fig. 4. Curves of (42). $CV_0 = 1$.

filters, in addition to statistics of the original neighboring pixels, the statistics of the filtered pixels are exploited [see (18)]. This extra information is used to increase the ENL. In fact, all filtered pixels $\hat{x}_i$ for different window sizes ($i=N, N-1, \ldots N_{\min}$) verify (18). $N_{\min}$ is the smallest number of samples [see Fig. 1(b)]. Since $\text{var}(\hat{x}_N) = x^2/N = 0$ for infinite N, the filtered pixel for infinite samples $\hat{x}_\infty$ corresponds to the parameter b' [see Fig. 1(b)]. In fact, for each pixel of the image, the vector $\hat{X} = (\hat{x}_N \, \hat{x}_{N-1} \ldots \hat{x}_{N_{\min}})$ can be generated by applying the original filter for $N, N-1 \ldots$, samples. Then, from the filtered images, the vector $\text{var}\hat{X} = (\text{var}\hat{x}_N \, \text{var}\hat{x}_{N-1} .. \text{var}\hat{x}_{N_{\min}})$ can also be defined. Finally, $\hat{x}_\infty$ is estimated by linear regression between the vectors $\hat{X}$ and $\text{var}\hat{X}$ [see Fig. 1(b)]. Theoretically, the ENL of the original filter is ENL($\bar{y}$) = N whereas the INLP filter one is infinite [i. e. ENL(b')>N]. As a result, (18) outperformed (2) in terms of speckle reduction. These outcomes will be verified in practice.

C. Bias Estimation

Equation (14) demonstrated also that (2) (i.e., the initial filter) is a biased estimate of the noise free pixel. This bias is due to insufficient homogeneous samples. In fact

$$\text{bias} = \bar{\hat{x}} - x = \frac{(\bar{y} - x)}{\text{var}(x)} \text{var}(\hat{x}) \tag{26}$$

where $\text{var}(x)$ is given in (4) and $\bar{\hat{x}}$ is the mean of the filtered homogeneous N pixels. In real data, the number of homogeneous pixels is finite. In this case, $x \neq \bar{y}$ and the original filter introduces the bias (26). For infinite samples, $x = \bar{y}$ and bias=0.

D. Correlation Between the Pixels

The correlation between the image's pixel values has an undesirable impact in the estimation of the useful information of SAR [31]–[32] and PolSAR data [33]. For example, in [33], the authors demonstrated that the correlation between the pixels increased the biases in the radar cross section, the polarimetric complex correlations, the eigenvalues and the ENL. Spatial correlation between the pixels have many sources.
1) During the SAR image formation, the use of matched filters, such as Hamming windows, introduces a spatial correlation. Several methods have been introduced to remove such correlation [31]–[33].

2) The averaging operation in spatial domain corresponds to low-pass filtering in the frequency domain. This operation introduces a correlation between the pixels. In this article, this type of correlation between the pixels is discussed.

Fig. 2 displays the filtered image using the 5×5 boxcar filter (i.e., spatial averaging) and the 25-looks images (i.e., statistical averaging). Since SAR data are assumed to be ergodic, both filters ensured the same speckle reduction level (i.e., ENL=25) [see probability density functions (pdfs) in Fig. 2]. However, it is observable in 25-looking, the pixels remain independent. It has been reported in [34] that N-looks SAR images are not correlated. This effect is observable in Fig. 2(c) (25-looks statistical averaging). On the other hand, the spatial averaging introduces a blurring effect (i.e., a correlation between the pixels). In this study, the performances of the improved INLP and the original filter are compared regarding this criterion (i.e., reducing a correlation between the pixels).

E. Spatial Detail Preservation

To study the variation of b' (18), two U and V random vectors having K elements and normal distributions have been simulated where $K = 50$ and $\min(U)=0$ and $\max(U)=1$. The parameter b' is computed using (18). The process has been repeated 10 000 times. Fig. 3 displays the histogram of the parameter b'. Then, it can be verified that

$$\min(U) < b' < \max(U). \tag{27}$$

In fact, it is well known in speckle filtering that the spatial detail preservation of edges, lines, textures, point targets, …. decreases with the increase of the window size. Consequently, in the filtered pixel vector $U=\hat{X} = (\hat{x}_N \quad \hat{x}_{N-1} \quad \ldots)$, $\hat{x}_N$ ensured the worst spatial detail preservation and $\hat{x}$ (i.e., original pixel) preserved it perfectly. When processing a pixel of a spatial detail, two cases can happen as follows.
1) The pixel value is small compared to its neighbor ones [i.e., dark pixel (line, edge, texture)]. In this case, $\min(U) = \hat{x}_1 < b' < \max(U) = \hat{x}_N$. Since $b' < \hat{x}_N$, the INLP filter better preserved the spatial detail.
2) The pixel value is high compared to its neighbor ones (i.e., high return of a line, edge, texture, point target). In this case, $\min(U) = \hat{x}_N < b' < \max(U) = \hat{x}_1$. Since $b' > \hat{x}_N$, the INLP filter better preserved the spatial detail.

For more explanation, let consider the case of the point target. Two cases can occur.
1) If the original filter smoothed the point target, then

$$\hat{x}_N < \hat{x}_{N-1} < \ldots < \hat{x}_{N\min} \tag{28}$$

and according to (27)

$$\hat{x}_N = \hat{x}_{N-1} = \ldots = \hat{x}_{N\min} = y. \tag{29}$$

As a result, since $b' > \hat{x}_N$, the INLP filter ensured higher spatial detail preservation than the original filter.
1) If the filter preserved the point target, then

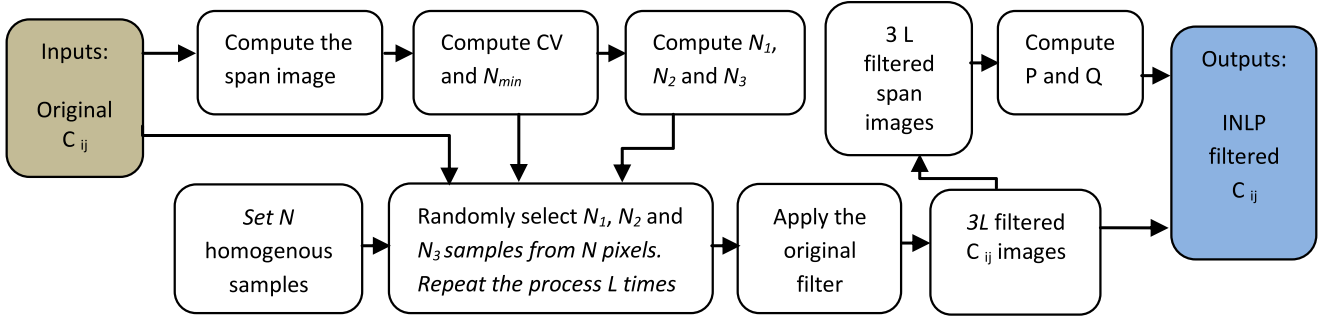$$\hat{x}_N = \hat{x}_{N-1} = \ldots = \hat{x}_{N\min} = y \tag{30}$$

Fig. 5. Flowchart of the INLP filter.

and

$$b' = \bar{U} = y \text{ (see (14))} . \tag{31}$$

As a result, the INLP filter preserved also the point target.

In conclusion, the INLP filter theoretically provided better spatial detail preservation than of the initially applied filter. These theoretical outcomes will be verified also in practice. It is noticed that the minimum number of samples used in the linear regression is 3. The use of two samples ($\hat{x}_1$ and $\hat{x}_2$ with $\hat{x}_2 < \hat{x}_1$) degrades the spatial details since the linear regression is a decreasing function so $b' < \hat{x}_2$ [see Fig. 1(c)].

F. Preservation of the Polarimetric Information

To avoid the distortion of the polarimetric information, it has been recommended that all the elements of the covariance matrix should be filtered equally [1], [2], [18]–[29]. However, it can be observed in (18) that the filtered pixel b' is not linearly related to $U_i = \hat{x}_1$ due to the existence of the square values of $\hat{x}_1$ (i. e. variances). Then, (18) can be rearranged as follows:

$$b' = \bar{U}\left(1 - \frac{\bar{V}^2}{\overline{V^2} - \bar{V}^2}\right) + \frac{\bar{V}}{\overline{V^2} - \bar{V}^2} \frac{1}{M}\sum_{i=1}^{M} V_i U_i$$

$$= P\bar{U} + QU^t \tag{32}$$

where the scalar P is

$$P = 1 - \frac{\bar{V}^2}{\overline{V^2} - \bar{V}^2} \tag{33}$$

and the vector Q is

$$Q = \frac{1}{M}\frac{\bar{V}}{\overline{V^2} - \bar{V}^2}V. \tag{34}$$

To ensure a linearity between b' and $U_i = \hat{x}_i$, the parameters P and Q should be the same for all the elements of the covariance matrix. In this study, the performances of the improved INLP and the original filter are also compared regarding the criterion of the preservation of the polarimtric information.

1) Computation of P and Q. Choice of the Reference Image: To ensure the polarimetric information preservation, the INLP technique is applied to all elements of the covariance matrix using the same parameters P and Q computed from a reference image. In the literature, the common used reference image is the *span* [1], [2], [18]–[29]. Hence, the parameters P and Q are

estimated using the *span* image and introduced in (32) to filter all the elements of the covariance matrix equally.

G. Computational Complexity

After the application of one filter, the INLP is applied in a second stage to enhance the filtering performance. This operation multiplied the CP by the factor $M = N - N_{\min} + 1$ where M is the number of the processed samples used in the linear regression. To alleviate this limitation, the number of the processed samples could be reduced. In fact, instead of using ($N-N_{\min}+1$) samples, three samples are sufficient to perform the linear regression. As a result, the complexity of the procedure is extremely reduced especially in high M. The number of samples selected are $N_1 = N$, $N_3 = N_{\min}$ and $N_2 = (N_1+N_3)/2$. Hence, $\hat{X} = (\hat{x}_{N1} \quad \hat{x}_{N2} \quad \hat{x}_{N3})$. A good choice of the parameter $N_{\min}$ is crucial. In fact, $N_{\min}$ adjusted the variability extent introduced in the linear regression. By manually selecting low $N_{\min}$, fine details are better preserved at the cost of speckle reduction. Conversely, augmenting $N_{\min}$ gave better speckle reduction since the linear regression enclosed little information about fine features but spatial details are not enhanced. To fix this issue, the parameter $N_{\min}$ is adapted to the variability of the processed scene. Hence, the coefficient variation CV of the original data is employed to estimate the variability of the pixels

$$\text{CV} = \frac{\text{std}(y)}{\text{mean}(y)} \tag{35}$$

$$\text{CV} \geq 1 \tag{36}$$

$$\text{CV} - 1 \geq 0. \tag{37}$$

To normalize the last expression, hyperbolic tangent function is applied [18]–[19]

$$0 \leq \tanh\left(\text{CV} - 1\right) \leq 1 \tag{38}$$

$$0 \leq 1 - \tanh\left(\text{CV} - 1\right) \leq 1. \tag{39}$$

This transformation is applied to make N_{min} is decreasing function of CV.

Then

$$1 \leq \left[(N - 3)\right)\left(1 - \tanh\left(\text{CV} - 1\right)\right)] + 1 \leq N - 2. \tag{40}$$
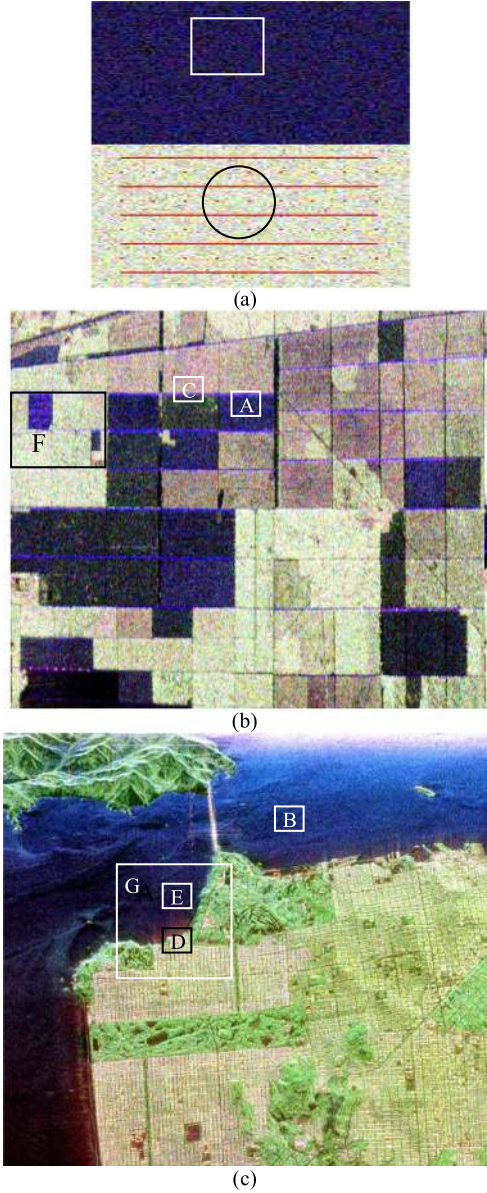
(a)

(b)

(c)

Fig. 6. Pauli coded images. (a) Simulated image: Ground truth $C_{\text{volume}}(C_{11} = 56, C_{12} = -2+9i, C_{13} = -17-5.16i, C_{22} = 59, C_{23} = 4+10i, C_{33} = 51)$, $C_{\text{suface}}(C_{11} = 2, C_{12} = -0.005+0.0178i, C_{13} = 2+0.004i, C_{22} = 0,0093, C_{23} = -0.007-0.017i, C_{33} =)$, $C_{\text{diplane}}(C_{11} = 3000, C_{12} = 0, C_{13} = -3000, C_{22} = 0, C_{23} = 0, C_{33} = 3000)$. (b) Les-Landes, b) San Fransico bay. A and B were selected to quantify the speckle reduction level. The zones C (line), D and E (point) were selected to study the ability of the filters to preserve spatial details preservation. The zones F and G are used for visual inspections.

Finally

$$1 \le N_{\min} = (N - 3) \left[1 - \left(\tanh m \left(\frac{\text{CV}}{\text{CV}_0} - 1 \right) \right)^n \right]$$
$$+ 1 \le N - 2 \qquad (41)$$

$$CV_0 = \frac{1}{\sqrt{ENL_0}} \qquad (42)$$

where m and n are two tuning parameters. ENL_0 is the ENL of the raw data. Fig. 4 displays the curves $N_{\min}$ as a function of CV for various m and n. It can be observed that the parameters m
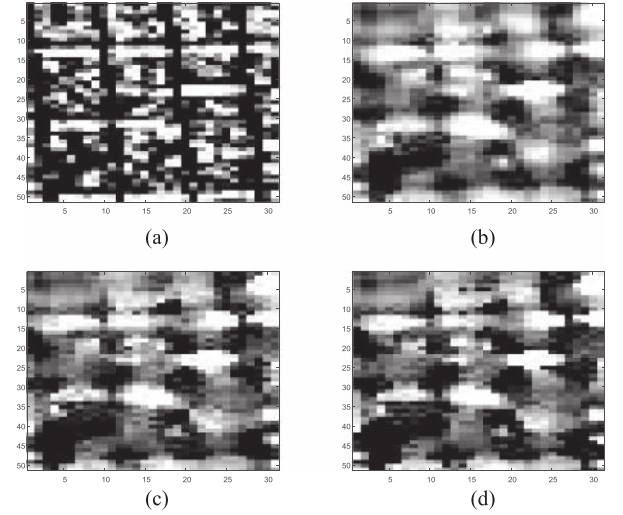

(a)   (b)

(c)   (d)

Fig. 7. Span images D zone. (a) Speckled image. (b) Original filter 5×5 sigma. (c) Original INLP. (d) Improved INLP.

(a)   (b)

(c)

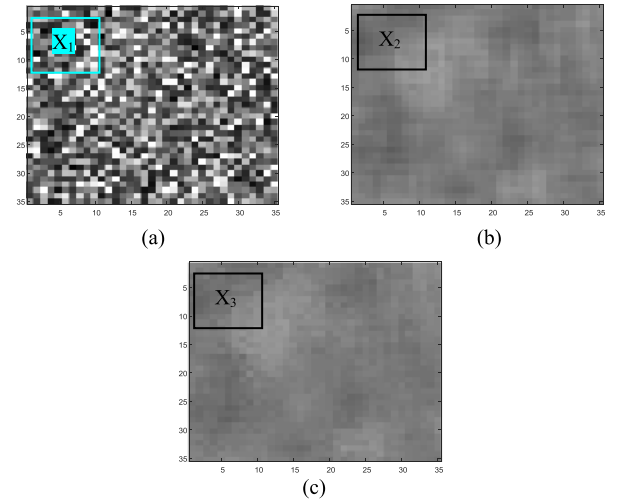Fig. 8. Span images simulated zone. (a) Speckled image. (b) Original filter 7×7 Boxcar. (c) Improved INLP.

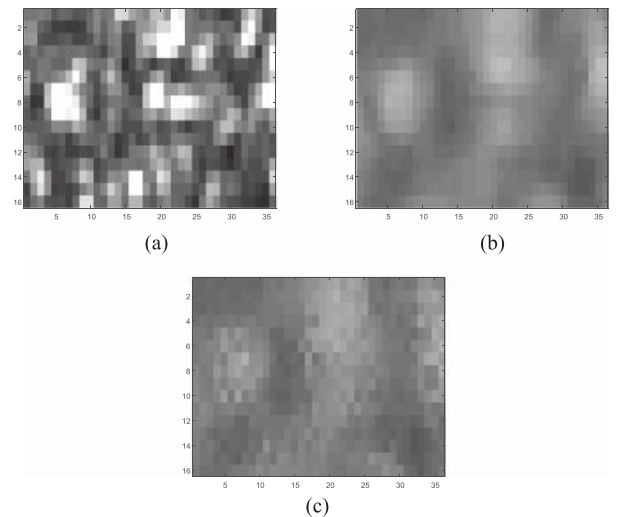(a)   (b)

(c)

Fig. 9. Span images A zone. (a) Speckled image. (b) Original filter 7×7 sigma. (c) Improved INLP.

and n control the decrease smoothness of the curves $N_{\min}$(CV). In this article, $m = 1$ and $n = 4$. In homogeneous areas, CV is low, $N_1 = N$, $N_2 = N\text{-}1$ and $N_3 = N\text{-}2$ so that speckle reduction is emphasized. In heterogeneous areas, CV is high, $N_{\min} = 1$ (i. e. original pixel) so that $N_1 = N$, $N_2 = (N\text{+}1)/2$ and $N_3 = 1$. In this case, spatial detail preservation is emphasized.

In this article, the performances of the improved INLP and the original filter are also compared regarding the criterion of the CP.

H. Practical Implementation of the Improved Polarimetric INLP Filter

The objective of this section is to propose a procedure to implement (32) in practice. For each pixel of the image which characterized by its covariance matrix.

i)   Define the span image.
ii) Set the neighborhood W containing N samples (i. e. N covariance matrices).
iii) Compute $CV(span)$ (35) and $N_{\min}$ (41).
iv) Compute N_1, N_2, and N_3.
v)   Randomly select N_i samples, where $N_i = N_1, N_2$ and N_3. The central pixel must be present for each N_i samples.
vi) Apply the original filter to all sets of N_i samples. So that each pixel of one polarimetric channel is represented by the vector $U = \hat{X} = (\hat{x}_{N1} \quad \hat{x}_{N2} \quad \hat{x}_{N3})$.
vii) Repeat steps v and vi L times to obtain sufficient samples. Each pixel of one polarimertric channel is represented by the vector U containing $M = 3L$ pixels. It is noticed that real and imaginary parts of the off-diagonal elements were filtered separately.
viii) Repeat the steps ii to vii for the entire pixels. Hence, for each polarimetric channel, $3L$ filtered images are obtained.
ix) Compute the filtered span images (i.e., $3L$ images).
x)   From each filtered span image, compute the variance images using the neighborhood W. Only pixels within the sigma range are selected to compute the variances (sigma=0.6 [24]). $3L$ additional images containing the variances of each filtered span image are obtained.
xi) Compute the parameters P (33) and Q (34) of each pixel.
xii) Compute the improved INLP filtered value of each polarimetric channel pixels using (32). Define the filtered covariance matrix and compute the derived polarimetric parameters such as the Cloude /Pottier parameters (i.e., the entropy H, the anisotropy A and the alpha angle α [35])

The implementation of the proposed INLP filter is also summarized by the flowchart of Fig. 5. The appendix A1 describes the algorithm of the proposed INLP filter. For more comprehension of the improved INLP filter, let consider the $5{\times}5$ boxcar as initial filter. Having a speckled PolSAR image as input of the INLP filter, the improved INLP is given: step i, compute the span image. Step ii, $N=25$. Step iii, let assume filtering a homogeneous area, CV=1 and $N_{\min} = 23$. Step iv, $N_1 = 25$, $N_2 = 24$ and $N_3 = 23$. Step v, from the 25 pixels, choose one element of the covariance matrix and randomly select 25, 24

and 23 samples. Step vi, average the selected pixels, we obtain the filtered pixels $\hat{x}_{25}$, $\hat{x}_{24}$, and $\hat{x}_{23}$. Repeat the last process L times. We obtain, L filtered pixels $\hat{x}_{25}$ (all have the same values), L different pixels $\hat{x}_{24}$ and L different pixels $\hat{x}_{23}$. Repeat the process for all the element of the covariance matrix and for all pixels of the image. Step ix, compute the filtered span images. Step x, compute the variances of the 3L span images using $5{\times}5$ window. Step xi, compute the parameters P and Q of each pixel of the image. Step xii, compute the improved INLP filtered pixel.

In this article, the boxcar and the sigma [24] filters are implemented as initial filters. However, the extension of the proposed method to the majority of the existing spatial filtering techniques is straightforward. In fact, the spatial filters differ generally in the manner of selecting the neighboring homogeneous pixels (e.g., edge aligned windows [2], the scattering model-based method [23], sigma range [24], scattering mechanism, and the intensity information [25], homogeneity measurement [26], NL [6]–[11], region growing [5], etc.). After that, these selected pixels are usually averaged or processed by the MMSE filter. Both strategies are implemented in this article (i.e., boxcar and sigma filter). Consequently, when applying any initial filter, the unique change in the INLP procedure resides in the selection of the N initial pixels.

III. EXPERIMENTAL RESULTS

$$C = \begin{pmatrix} 5.56 & -0.2 + 0.9i & -1.9 - 0.5i \\ -0.2 - 0.9i & 599 & 0.4 + i \\ -1.9 + 0.5i & 0.4 - i & 5.1 \end{pmatrix} \quad (43)$$

To assess speckle reduction quantitatively, two simulated images have been generated. In the first image, an extended homogeneous area containing 10 000 samples characterized by the covariance matrix (43) has been simulated. In the second simulated image, two kinds of speckled extended homogeneous areas corresponding to surface scattering and volume scattering have been generated [see Fig. 6(a)]. In addition, two deterministic targets corresponding to diplane scattering and characterized by high backscattering power have been introduced for spatial detail preservation assessment. The zones in the square and the circle are used to assess the speckle reduction and spatial detail preservation, respectively. The process of PolSAR data generation is given in [36]. In addition, two real airborne PolSAR images have been also tested. The first are the single look Les-Landes data having rectangular zones containing trees with different ages [see Fig. 6(b)]. The second are the San Francisco Bay PolSAR L-band four-look data [see Fig. 6(c)]. The image contains various typical scattering mechanisms: surface scattering (ocean); high returns from double bounce and point scatterings (city area); and volume scattering (park areas). The real data were acquired by the National Aeronautics and Space Administration Jet Propulsion Laboratory Airborne SAR.

A. Evaluation of PolSAR Speckle Filtering

The equivalent number of looks ENL is selected to evaluate the performances of different speckle filtering algorithms

TABLE I
RESULTS ORIGINAL VERSUS IMPROVED INLP

	ENL B zone	EPD_H	EPD_V
Sigma 5×5 (sigma=0.95)	42	0.6536	0.6772
INLP (Nmin=23, L=40)	54	0.6675	0.6915
Improved INLP (L=40)	54	0.6830	0.7078

quantitatively in terms of speckle reduction. The spatial detail preservation is evaluated by the edge preservation (EPD) [37]. The horizontal EPD is:

$$\text{EPD}_H = \frac{\sum\limits_{m,n} |\hat{x}(m,n)/\hat{x}(m,n+1)|}{\sum\limits_{m,n} |y(m,n)/y(m,n+1)|}. \quad (44)$$

To compute EPD_V, the indexes $(m,n+1)$ in (44) are replaced by $(m+1,n)$. The EPD range is $0 < \text{EPD} < 1$. A high EPD value means good spatial detail preservation. Diverse parameters are considered to assess PolSAR speckle filtering. The *span* is chosen to calculate the ENLs and EPDs. The amplitudes, the phases of the complex correlation coefficients and Cloude–Pottier parameters are used to evaluate PolSAR data preservation. The span and Pauli coded images are also considered for visual inspections.

B. Effects of the Adaption of N_{min} to the Variability of the Scene

The parameter $N_{\min}$ is a tuning factor which adjusts the performance of the filter. High $N_{\min}$ favors the speckle reduction whereas low $N_{\min}$ favors the spatial detail preservation [31].

For example, for $N_{\min} = 23$, the samples used in the linear regression in classical INLP are $\hat{X} = (\hat{x}_{25} \quad \hat{x}_{24} \quad \hat{x}_{23})$ i.e., 3 samples, independently the variability of scene. When $N_{\min}$ is adapted to the variability of the scene as in (32), in homogeneous areas, $\hat{X} = (\hat{x}_{25} \quad \hat{x}_{24} \quad \hat{x}_{23})$ i.e., $N_{\min} = 23$. In this case, the improved INLP gives the same speckle reduction level as the classical version. Nevertheless, in spatial details (e. g. point target), CV is high, $N_{\min} = 1 < 23$ and $\hat{X} = (\hat{x}_{25} \quad \hat{x}_{12} \quad \hat{x}_1)$. As a result, the improved INLP outperformed the classical version in terms of the spatial detail preservation. The performances of the INLP filter are studied for both strategies (i.e., $N_{\min} = 23$ and $N_{\min}$ is adapted to the variability of the scene).

Fig. 7 displays the filtered span images of D zone. It can be observed that the improved INLP outperformed the original version in terms of spatial detail preservation. Both filters gave the same speckle reduction level and display better filtering performances than the original filter (i.e., sigma filter). Quantitative results agree with visual inspections $(\text{EPD}_{H(\text{improved INLP})} = 0.6830 > \text{EPD}_{H(\text{INLP})} = 0.6675 > \text{EPD}_{H(\text{sigma})} = 0.6536)$ and $\text{ENL}_{(\text{improved INLP})} = 54 = \text{ENL}_{(\text{INLP})} = 54 > \text{ENL}_{(\text{sigma})} = 42$ (see Table I).

To increase the spatial detail preservation of the original INLP, low $N_{\min}$ values should be introduced. However, this choice will reduce the speckle reduction level and increase the CP since the number of the processed samples is increased. In the last experiment, the sigma filter with a window size W=5×5 is implemented. In the literature larger window sizes are generally

TABLE II
RESULTS SIMULATED DATA 1

	ENL
Boxcar 7×7	127
Improved INLP (L=40)	161

TABLE III
RESULTS SIMULATED DATA 2

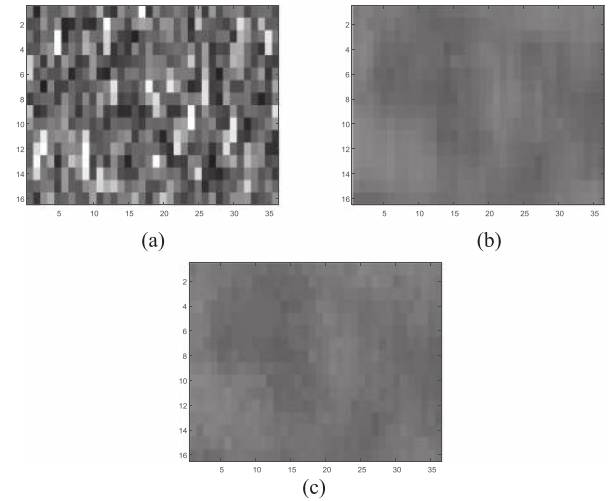|	ENL	EPD_H	EPD_V
Sigma filter 13×13 (sigma=0.9)	31	0.4847	0.4538
Improved INLP(L=40)	34	0.4953	0.4657
MSF	158	0.4917	0.4556

Fig. 10.   Span images B zone. (a) Speckled image. (b) Original filter 7×7 sigma. (c) Improved INLP.

TABLE IV
RESULTS ONE-LOOK DATA

	ENL	EPD_H	EPD_V
Sigma filter 7×7 (sigma=0.9)	25	0.8398	0.8183
Improved INLP(L=40)	32	0.8622	0.8426
MSF	32	0.8426	0.8204
NL Pretest	97	0.8266	0.8026

used (i.e., 7×7, 9×9 and 11×11). In these cases, the CP of the classical INLP becomes huge. Conversely, increasing the window size does not affect the CP of the improved INLP since three samples are always used $\hat{X} = (\hat{x}_{N1} \quad \hat{x}_{N2} \quad \hat{x}_{N3})$.

C. Comparisons with the Initial Filter

1) Speckle Reduction: Table II gives the ENL of the span of the simulated data 1 obtained by the studied filters. It can be observed that the improved INLP filter outperformed the initially applied filter (i.e., 7×7 boxcar) in terms of speckle reduction (i.e., ENL=161>127). Hence, averaging N homogeneous pixels only (i.e., boxcar or multi-looking) is not the optimal scenario. The same N pixels can be exploited to increase the ENL. The same outcomes can be verified for one-look and four-looks homogeneous areas (see the filtered simulated 1, simulated 2, A and B zones in Figs. 8–11 and Tables II, to V, respectively) where the improved INLP filter outperformed the initially applied filter
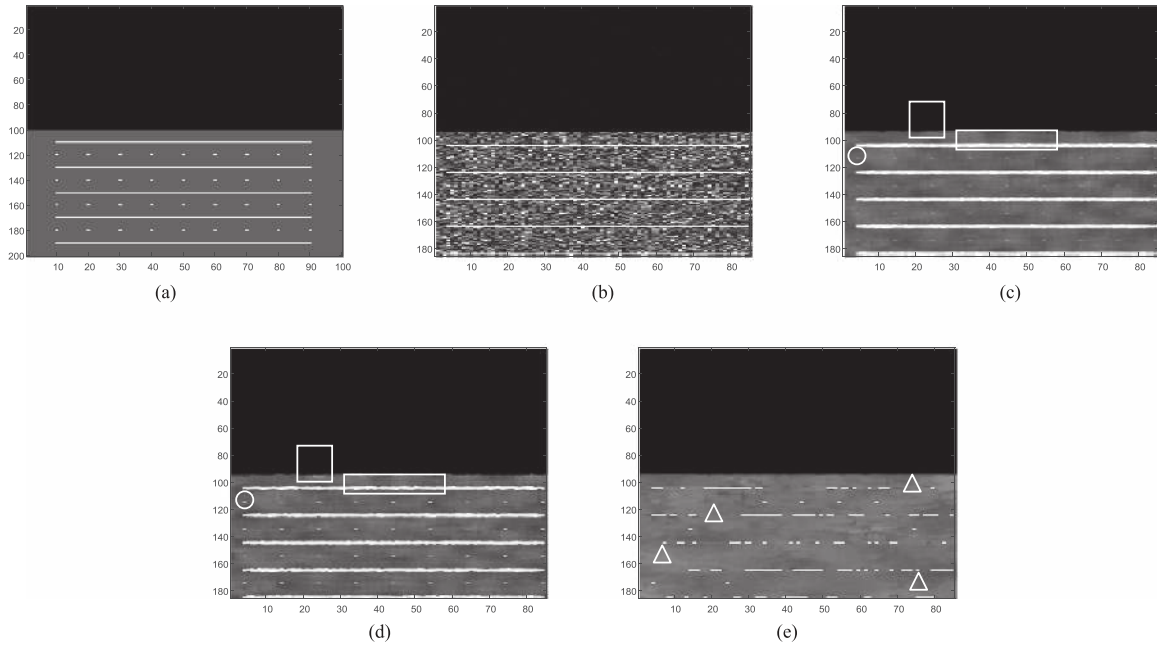
Fig. 11.   Span of simulated image. (a) Ground truth. (b) Speckled image. (c) Original filter 7×7 sigma. (d) Improved INLP. (e) MSF filter.
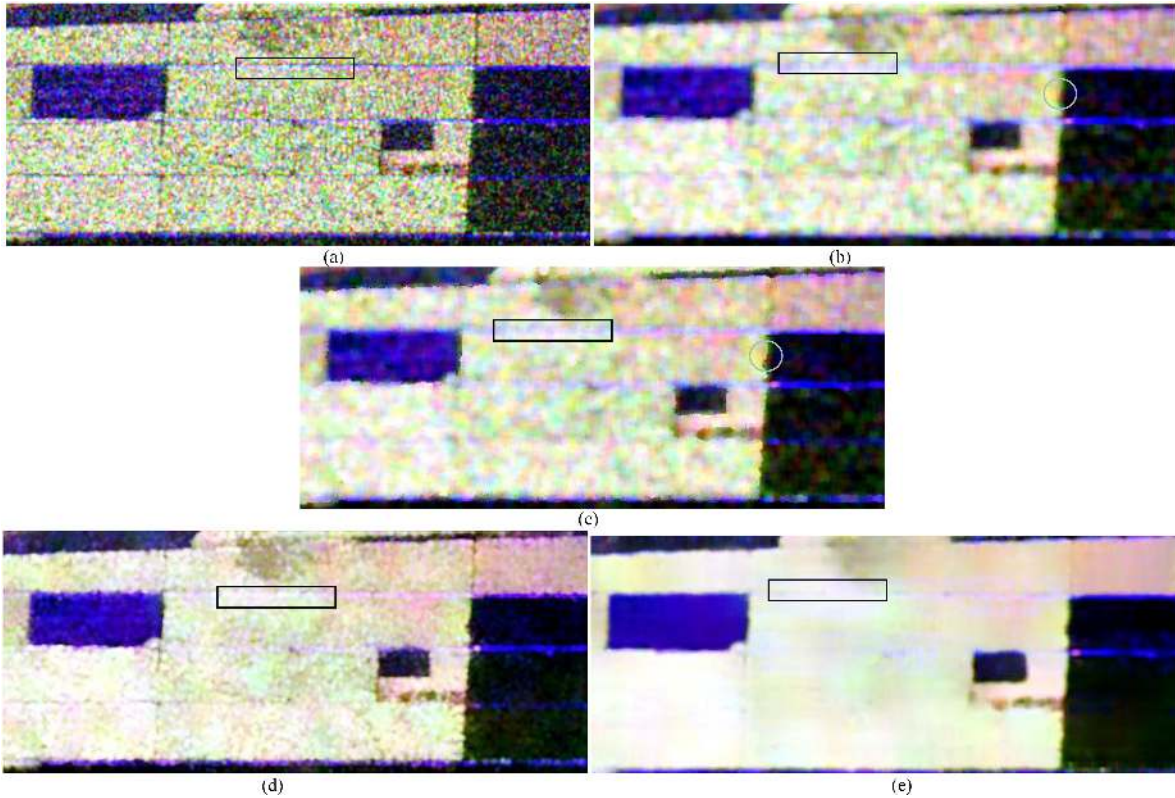

Fig. 12.   Pauli coded images F zone. (a) Speckled image. (b) Original filter 7×7 sigma. (c) Improved INLP. (d) MSF filter. (e) NL Pretest filter.

(7×7 sigma) in terms of speckle reduction. Hence, (32) ensured higher speckle reduction level than the original filter.

2) Bias Estimation: In real data, the ground truth (i.e., the noise free pixel x) is not available. To evaluate the ability of (18) to assess the biases introduced by (2), the simulated data are used. Table V gives the true (i. e. $\hat{\bar{x}}_N - x$) and the estimated

[i.e.,$(\bar{y} - x)\mathrm{var}(\hat{x})/\mathrm{var}(x)$] biases introduced by 5×5 boxcar filter estimated in *hh* intensity image for various numbers of homogeneous pixels. It can be perceived that 5×5 boxcar filter introduced minus biases that can be assessed by (26).

3) Correlation Between the Pixels: Figs. 8–10 visually show the filtered span images of the studied homogeneous zones (i.e.,
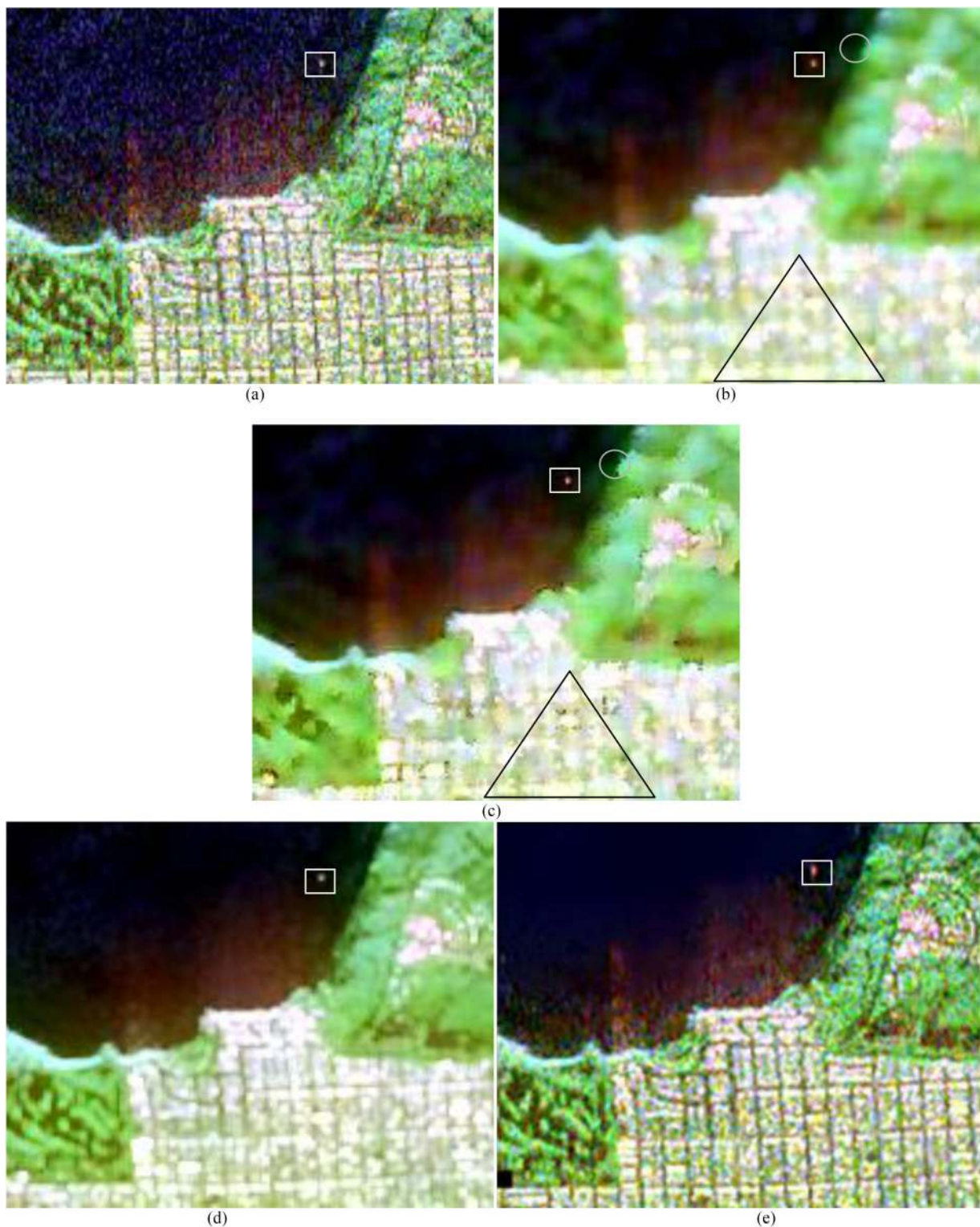
Fig. 13. Pauli coded filtered images of San Francisco Bay image (G zone). (a) Speckled image. (b) Original filter 5×5 sigma. (c) Improved INLP. (d) MSF filter. (e) NL Pretest filter.

simulated, A and B zones, respectively). The original pixels are supposed to be independent [34] [see Figs. 8(a), 9(a), and 10(a)] with an identity autocorrelation matrix (see appendix A2). However, it is observed that the spatial filtering (i.e., boxcar and MMSE) introduces statistical correlation (i.e., a blurring effect)

to the filtered pixels. The application of the INLP filter visually shows a clear reduction of the correlation introduced by the original filters. For quantitative evaluation, the autocorrelation matrices of X_1, X_2 and X_3 zones in Fig. 8 have been computed (see appendix A2). It can be observed that the INLP filter
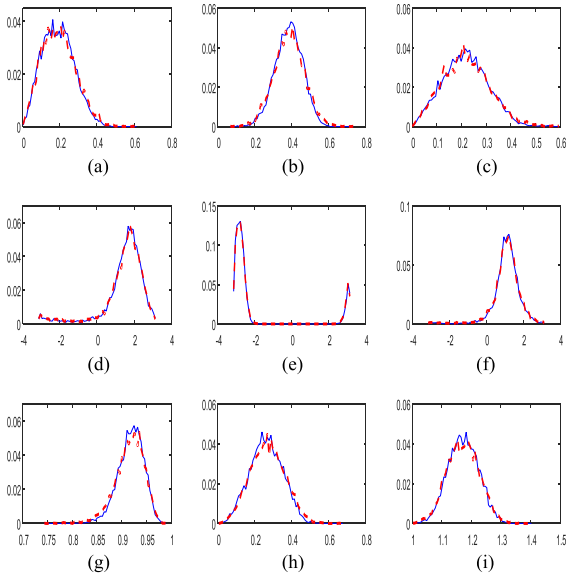
Fig. 14. PDFs of the parameters of the covariance matrix of the simulated data. Blue lines: 7×7 Boxcar. Dashed red lines: improved INLP. (a) $|\rho_{12}|$, (b) $|\rho_{13}|$, (c) $|\rho_{23}|$, (d) $\varphi_{12} \, rad$, (e) $\varphi_{13} \, rad$, (f) $\varphi_{13} \, rad$, (f) $\varphi_{23} \, rad$, (g) *H*, (H) *A*, and (i) $\alpha \, rad$.
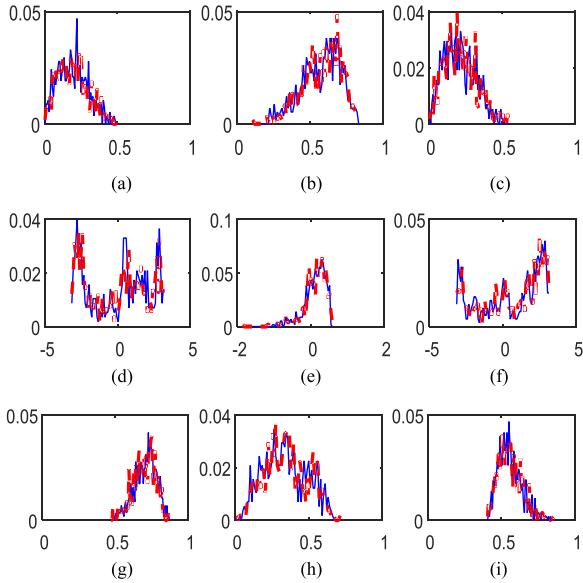

Fig. 15. PDFs of the parameters of the covariance matrix of the real data [i.e., A zone of Fig. 5(a)]. Blue lines: 7×7 sigma filter. Dashed red lines: improved INLP. (a) $|\rho_{12}|$, (b) $|\rho_{13}|$, (c) $|\rho_{23}|$, (d) $\varphi_{12} \, rad$, (e) $\varphi_{13} \, rad$, (f) $\varphi_{13} \, rad$, (f) $\varphi_{23} \, rad$, (g) *H*, (H) *A*, and (i) $\alpha \, rad$.

TABLE V
RESULTS FOUR-LOOKS DATA

	ENL *A zone*	*EPD$_H$* *Point target*	*EPD$_V$* *Point target*
Sigma *7×7* **(sigma=0.95)**	96	0.8073	0.8183
Improved INLP(*L*=40)	123	0.8266	0.8388
MSF	125	0.8073	0.8183
NL Pretest	433	0.8384	0.8420

TABLE VI
RESULTS ONE-LOOK DATA

Homogeneous samples	*20×20*	*30×30*	*40×40*	*50×50*
$\overline{\hat{x}}_N - x$	0.079	-0.035	-0.127	-0.067
$\dfrac{(\overline{y} - x)}{\mathrm{var}(x)} \dfrac{x^2}{N}$	0.067	-0.002	-0.100	-0.052

produced lower correlation coefficient magnitudes than the original filter (i. e. boxcar) (see off-diagonal elements).

4) Spatial Detail Preservation: Fig. 11 displays the filtered span of the simulated PolSAR image. It can be observed that the improved INLP filter outperformed the original filter (i.e., sigma) in terms of spatial detail preservation. In fact, the edge (square), line (rectangle) and point target (circle) appeared more contrasted in Fig. 11(d) than those in Fig. 11(c). Figs. 12 and 13 display the filtered RGB Pauli coded images of B and G zones, respectively. It can be observed that the spatial resolution is considerably increased by the improved INLP filter. The lines (see rectangles) and edges (see circles) in Figs. 12(c) and 13(c) are more contrasted than those in Figs. 12(b) and 13(b), respectively. The point target E produced by sigma filter in Fig. 13(b) appears more blurred than the one produced by the INLP in Fig. 13(c)(see squared zones). The smoothing action in the textured areas in Fig. 13(c) is considerably reduced compared with the ones of Fig. 13(b) (see triangles). Tables III –V confirm the visual inspections where the improved INLP ensured higher EPDs than sigma filter. The filtered pixels with smaller window sizes ensured better spatial detail preservation than the original one. This information is exploited by the INLP via (32) to produce better spatial detail preservation than the original filter.

5) Polarimetric Information Preservation: Fig. 14 displays the pdfs of the covariance matrix elements of the simulated data. It can be observed that the overall polarimetric information i.e., phase differences, the coherences between polarimetric channels and Cloude/Pottier parameters [i.e., entropy H and alpha angle α] is maintained without introducing distortions or biases. Fig. 15 displays the pdfs of the covariance matrice elements of the real data (i.e., A zone). The whole polarimetric information and the statistical characteristics were also preserved.

Figs. 16 and 17 display the filtered entropy and alpha angle images of the simulated image, respectively. It can be observed that the improved INLP filter preserved the overall information of extended homogeneous areas with a clear amelioration of the polarimatric information of fine details. The lines and points are characterized by high returns from double bounce scatterings (*H* = 0 and α = 90 see ground truth). It can be observed that the sigma filter distorted these details whereas the improved INLP filter corrected this inaccuracy to a great extent.

Fig. 18 shows the filtered entropy and alpha angle images of Les-Landes image. It is obvious that the INLP filter preserved the whole polarimetric information with a notable increase in the spatial resolution in extended homogeneous areas (see circles) and a distinguished amelioration of the polarimetric information preservation of spatial details (see rectangles).
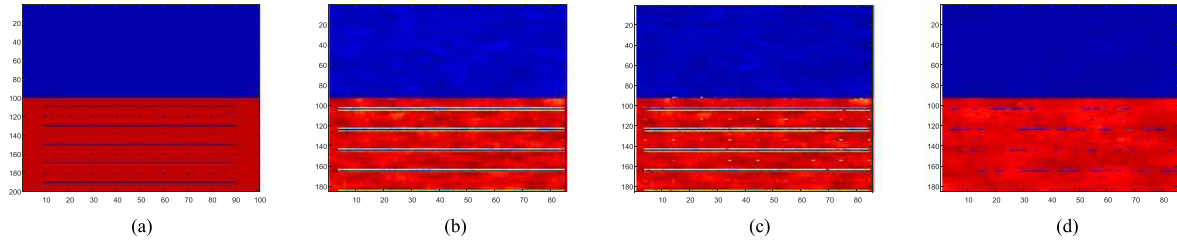
Fig. 16.   Entropy of simulated image. (a) Ground truth. (b) Original filter 7×7 sigma. (c) Improved INLP. (d) GMS filter.
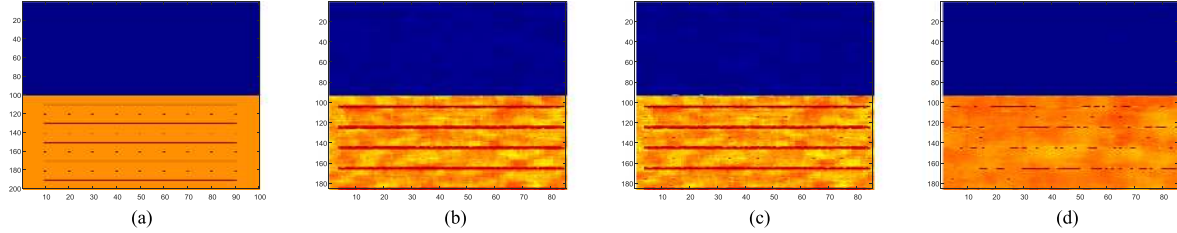

Fig. 17.   Alpha angle of simulated image. (a) Ground truth. (b) Original filter 7×7 sigma. (c) Improved INLP. (d) MSF filter.

Figs. 19 and 20 show the filtered entropy and alpha angle images of San Francisco Bay, respectively. It can be observed that the improved INLP filter preserved the overall information of extended homogeneous areas with a clear amelioration of the spatial resolution particularly in the city zone. The city is characterized by high returns from double bounce point scatterings ($H = 0$ and $\alpha = 90$). It can be observed that the improved INLP enhanced this information and retrieved the initially blurred fine details (see rectangles). The point target E ($H = 0$ and $\alpha = 90$) is situated in the sea where $H = 0$ and $\alpha = 0$. Normally, the entropy image is not able to discern the point target [see triangle in Fig. 19(a)]. The sigma filter preserved the polarimetric information of the point target ($H = 0$, blue color). Nevertheless, high entropy values are observed around the point target. This inaccuracy is due to the effect of mixing different scattering media [surface scattering (sea)+ double bounce(point target)] [27] and [36]. By applying the improved INLP filter, the effect of mixing different media around spatial details is reduced (see triangles). As a result, the improved INLP filter better preserved the polarimetric information of fine details than the initially applied filter.

D. Comparisons With the State-of-the-Art PolSAR Filters

In this article, it has been demonstrated that the INLP filter improved the performance of the initially applied filter (i.e., Lee sigma filter). To further assess the effectiveness of the improved INLP filter, two other updated PolSAR filters have been implemented for comparisons. Results are obtained using PolSARpro software [37]. In the INLP, the sigma filter was used as initial filter.

1) First Filter is the MSF filter [11]: Window size target 3, window size filter WSF=7, 11 and 15 for simulated, San Francisco bay and Les-Landes images, respectively, convergence threshold 0.1, shape parameter 1, sigma 0.9, spatial domain Kernel selection (Gaussian), range domain Kernel selection (Gaussian), central pixel estimation (MMSE), truncation parameter spatial domain 3 range domain 3.

The MSF produced very high speckle reduction level of simulated data (ENL=158). Nevertheless, the INLP produced better spatial detail preservation since many spatial details in the filtered MSF image disappeared [see triangles of Fig. 11(e)]. Quantitative outcomes agree well with visual interpretations where $\text{EPD}_{\text{V-INLP}} = 0.4657 > \text{EPD}_{\text{V-MSF}} = 0.4556$. It can be seen also that the INLP produced better polarimetric information preservation of fine details (see entropy and α images in Figs 16 and 17, respectively).

Les-Landes image: The INLP and MSF produced the same speckle reduction level (ENL=32). Visual inspections of Fig. 12(c) and 12(d) shows that the INLP outperformed the MSF in terms of spatial detail preservation. For example, the MSF smoothed the line in the rectangular zone to some extent. Quantitative outcomes agree well with visual interpretations where $\text{EPD}_{\text{H-INLP}} = 0.8622 > \text{EPD}_{\text{H-MSF}} = 0.8426$. Concerning the polarimetric information preservation, the INLP produced better resolution and better preserved fine details (see rectangles).

San Francisco Bay image: It can be observed that MSF and INLP gave the same speckle reduction level ($\text{ENL}_{\text{MSF}} = 125 \approx \text{ENL}_{\text{INLP}} = 123$). Concerning the spatial detail preservation, the INLP produced better preserved high returns backscattering, such as the point target (see squares) and double bounce reflections in the city area (see rectangles). On the other hand the MSF better preserved details of the park (see triangles). Concerning the polarimetric information preservation, the INLP produced better resolution and better preserved high return backscattering that are characterized by $H = 0$ and $\alpha = 0$ (see triangles and rectangles in Figs. 19 and 20).

2) Second Filter is the NL Pretest Filter [6]: Search window size 15×15, patch window size 3×3, K coefficient=10.
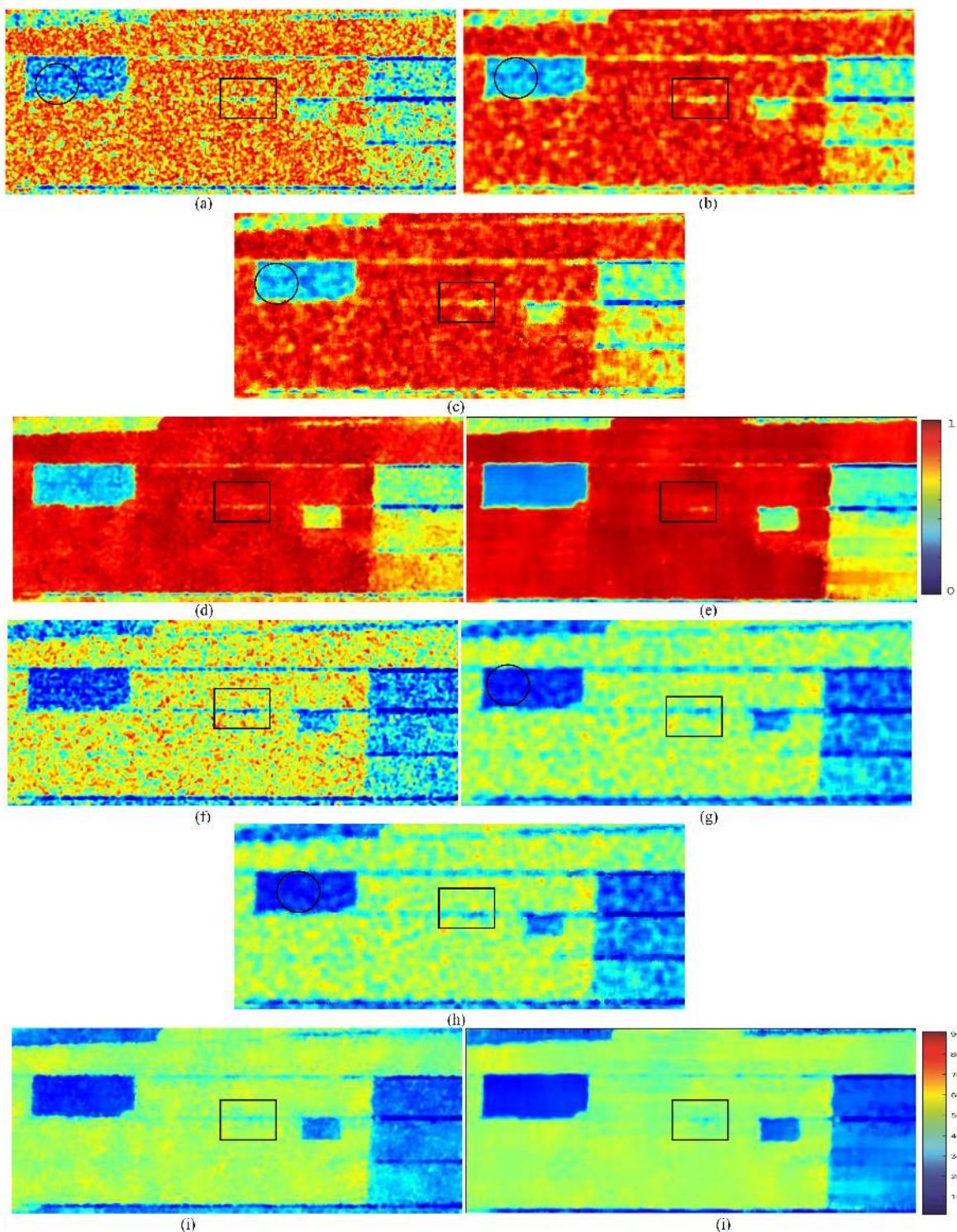
Fig. 18. Filtered F zone. (a) Entropy boxcar 3×3. (b) Entropy 7×7 sigma filter. (c) Entropy improved INLP. (d) Entropy MSF filter. (e) Entropy NLM filter. (f) Alpha boxcar 3×3. (g) Alpha 7×7 sigma filter. (h) Alpha improved INLP. (i) Alpha MSF filter. (j) Alpha NLM filter.

Les-Landes image (number of looks=1): The NL pretest filter ensured higher speckle reduction level (ENL_NL=97> ENL_INLP=32) at the detriment of preservation of the spatial details (EPD$_{\text{H-INLP}}$ = 0.8622>EPD$_{\text{H-NLM}}$ = 0.8426). These interpretations can be verified visually in Fig. 12 where the NL reduced the speckle to a great extent but the line (see rectangles) is considerably blurred. The NL ensured higher entropy and

alpha angle bias compensation level than INLP since it ensured higher speckle reduction level but the former better preserved the polarimetric information of the line (see rectangles in Fig. 18).

San Francisco Bay image (number of looks=4): The NL Pretest Filter ensured high speckle reduction level (ENL=631) and high preservation of the spatial details in the city and the park zones (EPD$_{\text{H}}$ = 0.8384) (see Fig. 13). However, it introduced
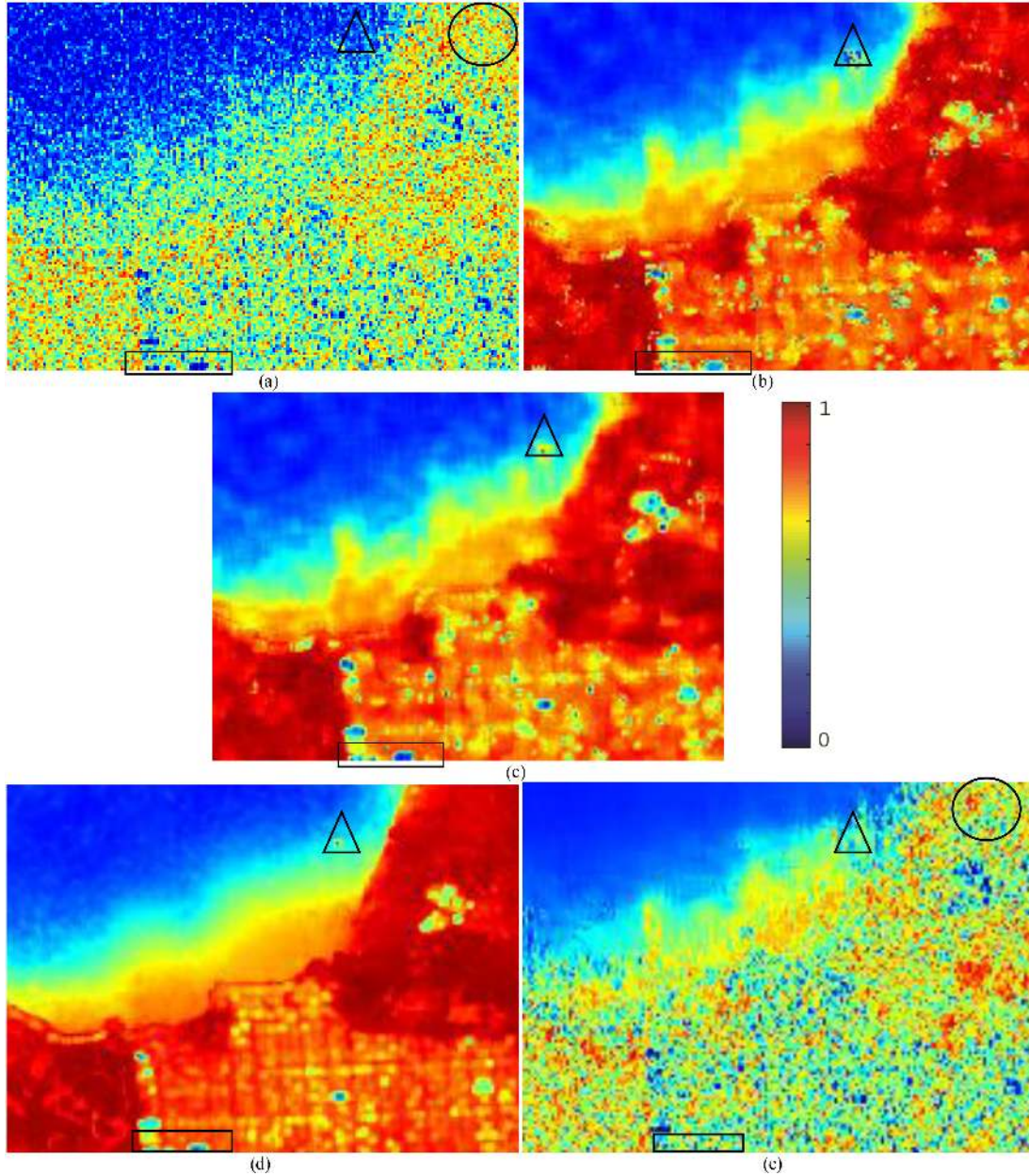
Fig. 19. Filtered G zone. (a) Entropy boxcar 3×3. (b) Entropy 7×7 sigma filter. (c) Entropy improved INLP. (d) Entropy MSF filter. (e) Entropy NLM filter.

artifacts (see arrow). On the other hand, the INLP ensured better speckle reduction in the park (see triangle). The last result can be verified in the filtered entropy in Fig. 19(e) and alpha angle in Fig. 20(e) where the polarimetric information of the park is not filtered compared to the initial images in Figs. 19(e) and 20(e) (see circles), respectively.

3) Computational Complexity: In addition to the filtering performance, the CP of the PolSAR filter constitutes currently a great concern for practical implementations since for many of the new SAR systems (e.g., TerraSAR-X, Cosmo-SkyMed and Gaofen-3), the image dimensions are huge (i.e., higher than 10 000 × 10 000 pixels).

Let the size of the image be $N_x \times N_y$, the number of pixels in search window be N and the patch size be N'. The conventional spatial filters, such as refined Lee, Lee sigma, are the most computationally efficient methods among other better speckle filtering algorithms for huge datasets where CP is $O(N_x \times N_y \times N)$. The CP of the INLP filter is $CP_{INLP} = CP_1 + O(N_x \times N_y \times N \times R)$. CP_1 is the CP of the original filter and R is the number of the samples used in the linear regression. In the classical INLP (i.e., without adaptation of N_{min} to the variability of the scene), $R = (N\text{-}N_{min}+1) \times L$ while in the improved INLP, $R = 3 \times L$. The CP of the NLM filter is $O(N_x \times N_y \times N \times N')$. When the boxcar or sigma is used as initial filter $CP_{INLP} = R \times CP_1$. When the NLM is used as initial filter, for $N' = 3L$. $CP_{impINLP} = 2 \times CP_{NLM}$. When N is high (e.g., $N = 21 \times 21$ in NLM filters), the complex complexity of the improved INLP is considerably alleviated compared to the original version.
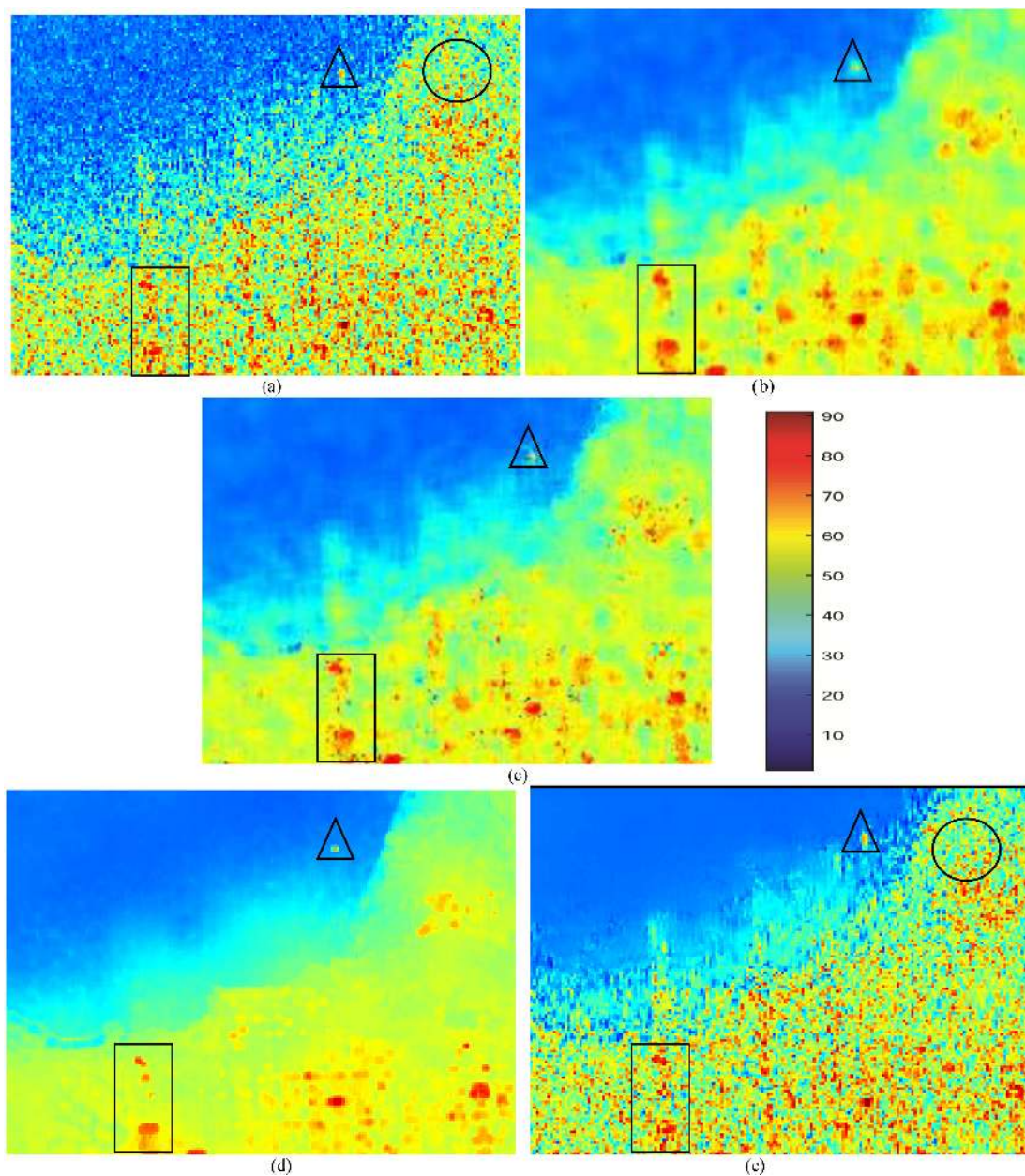
Fig. 20. Filtered G zone. (a) Alpha boxcar 3×3. (b) Alpha 7×7 sigma filter. (c) Alpha improved INLP. (d) Alpha MSF filter. (e) Alpha NLM filter.

E. Discussion

The essence of the INLP filter is the exploitation of the filtered pixels for various window sizes to improve the PolSAR filtering as given in (32). The theoretic outcomes showed that the INLP filter ameliorates the speckle reduction, improved the spatial details and preserved the polarimetric information of the initially applied filter. A procedure has been proposed for practical implementation of (32). This procedure can be the subject of many improvements. For example, the processed samples used in the linear regression are selected randomly. More adequate strategies could be used for the optimal selection of the representative samples. The experimental results using simulated and real PolSAR data validated the theoretical ones.

Hence, (31) outperforms classical spatial PolSAR filtering in terms of speckle reduction, spatial detail preservation, spatial resolution (or correlation between the pixels) and polarimatric information preservation. Nevertheless, the linear regression increased the CP. It is noticed that the INLP filter is not a totally independent filter. Its performance depends also on the choice of the original filter.

IV. CONCLUSION

In this article, the ability INLP filter in terms of speckle reduction and the spatial details preservation is demonstrated theoretically. The linear regression rule has been adapted to

PolSAR context in order to preserve the polarimetric information. In addition, the number of the processed pixels used in the linear regression is adapted to the variability of scene. This effort is recompensed by a reduction of the CP, an increase in speckle reduction and the improvement of the spatial details. Compared to the initial filter, the results demonstrate that the improved INLP filter performed higher speckle reduction level, enhanced the spatial details, increased the spatial resolution, reduced the correlation between the pixels and better preserved the polarimetric information. In future researches, the authors will focus on the optimization of the application of the INLP technique.

APPENDIX

A1: Algorithm INLP

Inputs

  F :initial filter
  f :function to compute N_{min}
  iImg(p,z),where elements are polarimetric data and p are 2D pixel coordinates.
  N: window size
  L:number of repetitions

Output: fImg (p,z) of filtered polarimetric data

```
sImg=SpanImage[iImg]
For k in 1..z
    For each p coordinate in iImg
        CV=coefficient_variation[sImg,N]
        Nmin=f[CV,N]
        N1=N; N3=Nmin;N2=(N1+N2)/2
        wImg=neighborhood[iImg,N,k]

        X̂ =[]
        For j in 1..L do
            For i in 1...3 do
                X(j,i)={x₁,...,x_Ni};  xᵢ randomly selected from wImg
                X̂ (j,i)=F[X(j,i),N]
                X̂ ={ X̂  X̂ (j,i)}
            end
        end
    end
end
For each p coordinate in iImg
    S_fImg(p,1..3L)=SpanImage[ X̂ ]
    V_fImg=variance [SfImg, N]
    U(1..L)= S_fImg(p,1..3L)
    V(1..L)= V_fImg(p,1..3L)
    Compute P
    Compute Q
    For k in 1..z
        Compute fImg(p,k)
    end
end
```

A2: The autocorrelation coefficients are computed using corrcoef(X) MATLAB function.

```
>> corrcoef(X₁)=
 1.0000  -0.0624  -0.2766   0.1067  -0.3654  -0.3913  -0.4390   0.4177  -0.1135  -0.2331
-0.0624   1.0000   0.1628  -0.5150   0.6424   0.1668  -0.1066  -0.1612   0.3406   0.0387
-0.2766   0.1628   1.0000  -0.0241   0.4573  -0.1491   0.3828  -0.3815  -0.4386  -0.0606
 0.1067  -0.5150  -0.0241   1.0000  -0.0268   0.0524   0.0874  -0.5675   0.0482   0.1390
-0.3654   0.6424   0.4573  -0.0268   1.0000   0.4354   0.5439  -0.6151   0.1037   0.3357
-0.3913   0.1668  -0.1491   0.0524   0.4354   1.0000   0.1371  -0.1597  -0.0536  -0.2503
-0.4390  -0.1066   0.3828   0.0874   0.5439   0.1371   1.0000  -0.4728  -0.2541   0.6714
 0.4177  -0.1612  -0.3815  -0.5675  -0.6151  -0.1597  -0.4728   1.0000  -0.2074  -0.5059
-0.1135   0.3406  -0.4386   0.0482   0.1037  -0.0536  -0.2541  -0.2074   1.0000   0.2978
-0.2331   0.0387  -0.0606   0.1390   0.3357  -0.2503   0.6714  -0.5059   0.2978   1.0000
>> corrcoef(X₂)=
 1.0000   0.9753   0.9539   0.8569   0.6443  -0.2958  -0.6837  -0.7053  -0.7980  -0.8230
 0.9753   1.0000   0.9780   0.9115   0.7510  -0.1572  -0.5478  -0.5843  -0.7085  -0.7157
 0.9539   0.9780   1.0000   0.9512   0.7968  -0.0899  -0.5065  -0.5570  -0.6812  -0.6959
 0.8569   0.9115   0.9512   1.0000   0.9133   0.1847  -0.2515  -0.2993  -0.4409  -0.4780
 0.6443   0.7510   0.7968   0.9133   1.0000   0.4650   0.0504   0.0016  -0.1825  -0.2177
-0.2958  -0.1572  -0.0899   0.1847   0.4650   1.0000   0.8782   0.8568   0.7657   0.7203
-0.6837  -0.5478  -0.5065  -0.2515   0.0504   0.8782   1.0000   0.9927   0.9598   0.9540
-0.7053  -0.5843  -0.5570  -0.2993   0.0016   0.8568   0.9927   1.0000   0.9761   0.9599
-0.7980  -0.7085  -0.6812  -0.4409  -0.1825   0.7657   0.9598   0.9761   1.0000   0.9836
-0.8230  -0.7157  -0.6959  -0.4780  -0.2177   0.7203   0.9540   0.9599   0.9836   1.0000
>> corrcoef(X₃)=
 1.0000   0.8740   0.8433   0.7254   0.5094  -0.3917  -0.6505  -0.8491  -0.7985  -0.7826
 0.8740   1.0000   0.9632   0.7178   0.6363  -0.1650  -0.4648  -0.7099  -0.6799  -0.6652
 0.8433   0.9632   1.0000   0.6683   0.5949  -0.1651  -0.4494  -0.7248  -0.7067  -0.6500
 0.7254   0.7178   0.6683   1.0000   0.8330   0.2221  -0.0257  -0.3521  -0.2654  -0.2524
 0.5094   0.6363   0.5949   0.8330   1.0000   0.4858   0.2747  -0.1238  -0.0715  -0.0022
-0.3917  -0.1650  -0.1651   0.2221   0.4858   1.0000   0.9249   0.6777   0.7491   0.7919
-0.6505  -0.4648  -0.4494  -0.0257   0.2747   0.9249   1.0000   0.8528   0.8920   0.9338
-0.8491  -0.7099  -0.7248  -0.3521  -0.1238   0.6777   0.8528   1.0000   0.9537   0.9517
-0.7985  -0.6799  -0.7067  -0.2654  -0.0715   0.7491   0.8920   0.9537   1.0000   0.9779
-0.7826  -0.6652  -0.6500  -0.2524  -0.0022   0.7919   0.9338   0.9517   0.9779   1.0000
```

A2: Latex program of the proposed method is missing.

ACKNOWLEDGMENT

REFERENCES

[1] S. Lee and E. Pottier, *Polarimetric Radar Imaging From Basics to Applications*. Boca Raton, FL, USA: CRC Press, 2009.

[2] J. S. Lee, M. R. Grunes, and G. De Grandi, "Polarimetric SAR speckle filtering and its implication for classification," *IEEE Trans. Geosci. Remote Sens.*, vol. 37, no. 5, pp. 2363–2373, Sep. 1999.

[3] C. López-Martínez and X. Fàbregas, "Polarimetric SAR speckle noise model," *IEEE Trans. Geosci. Remote Sens.*, vol. 41, no. 10, pp. 2232–2242, Oct. 2003.

[4] C. López-Martínez and X. Fabregas, "Model-based polarimetric SAR speckle filter," *IEEE Trans. Geosci. Remote Sens.*, vol. 46, no. 11, pp. 3894–3907, Nov. 2008.

[5] G. Vasile, E. Trouve, J. S. Lee, and V. Buzuloiu, "Intensity-driven-adaptive-neighbourhood technique for polarimetric and interferometric parameter estimation," *IEEE Trans. Geosci. Remote Sens.*, vol. 44, no. 6, pp. 1609–1621, Jun. 2006.

[6] J. Chen *et al.*, "Nonlocal filtering for polarimetric SAR data: A pretest approach," *IEEE Trans. Geosci. Remote Sens.*, vol. 49, no. 5, pp. 1744–1754, May 2011.

[7] L. Torres, S. J. S. Sant'anna, C. Da Costa Freitas, and A. C. Frery, "Speckle reduction in polarimetric SAR imagery with stochastic distances and nonlocal means," *Pattern Recognit.*, vol. 47, no. 1, pp. 141–157, Jan. 2014.

[8] C.-A. Deledalle, L. Denis, F. Tupin, A. Reigber, and M. Jäger, "NL-SAR: A unified nonlocal framework for resolution-preserving (Pol)(In)SAR denoising," *IEEE Trans. Geosci. Remote Sens.*, vol. 53, no. 4, pp. 2021–2038, Apr. 2015.

[9] G. Liu and H. Zhong, "Nonlocal means filter for polarimetric SAR data despeckling based on discriminative similarity measure," *IEEE Geosci. Remote Sens. Lett.*, vol. 11, no. 2, pp. 514–518, Feb. 2014.

[10] H. Zhong, J. Zhang, and G. Liu, "Robust polarimetric SAR despeckling based on nonlocal means and distributed Lee filter," *IEEE Trans. Geosci. Remote Sens.*, vol. 52, no. 7, pp. 4198–4210, Jul. 2014.

[11] F. Lang, J. Yang, D. Li, L. Shi, and J. Wei, Mean-Shift-Based speckle filtering of polarimetric SAR data," *IEEE Trans. Geosci. Remote Sens.*, vol. 52, no. 7, pp. 4440–4454, Jul. 2014.

[12] L. I. Rudin, S. Osher, and E. Fatemi, "Nonlinear total variation based noise removal algorithms," *Phys. D, Nonlinear Phenomena*, vol. 60, no. 1–4, pp. 259–268, Nov. 1992.

[13] X. Nie, H. Qiao, and B. Zhang, "A variational model for Pol-SAR data speckle reduction based on the Wishart distribution," *IEEE Trans. Image Process.*, vol. 24, no. 4, pp. 1209–1222, Apr. 2015.

[14] X. Nie, H. Qiao, B. Zhang, and X. Huang "A nonlocal TV-Based variational method for PolSAR data speckle reduction," *IEEE Trans. Image Process.*, vol. 25, no. 6, pp. 2620–2634, Jun. 2016.

[15] S. Foucher, M. Beaulieu, M. Dahmane, and F. Cavayas, "Deep speckle noise filtering," in *Proc. Int. Geosci. Remote Sens. Symp.*, 2019, pp. 5311–5314 .

[16] S. Foucher, M. Beaulieu, F. Cavayas, and M. Dahmane, "Revising an iterative speckle filtering technique," in *Proc. Int. Geosci. Remote Sens. Symp.*, 2019, pp. 5213–5216.

[17] L. Denis, C. A. Deledalle, and F. Tupin, "From patches to deep learning: Combining self-similarity and neural networks for SAR image despeckling," in *Proc. Int. Geosci. Remote Sens. Symp.*, 2019, pp. 5113–5116.

[18] M. Yahia, T. Ali, M. M. Mortula, R. Abdelfattah, S. El Mahdi and N. S. Arampola, "Enhancement of SAR speckle denoising using the improved IMMSE filter," *IEEE J. Sel. Topics Appl. Earth Observ. Remote Sens.*, vol. 13, pp. 859–871, Feb. 2020.

[19] M. Yahia, T. Ali, and M. M. Mortula, R. Abdelfattah, and S. El Mahdy "Polarimetric SAR speckle reduction by hybrid iterative filtering," *IEEE Access*, vol. 8, no. 1, Dec. 2020.

[20] J. S. Lee, M. R. Grunes, and S. A. Mango, "Speckle reduction in multipolarization and multifrequency SAR imagery," *IEEE Trans. Geosci. Remote Sens.*, vol. 29, no. 4, pp. 535–544, Jul. 1991.

[21] S. Goze and A. Lopes, "A MMSE speckle filter for full resolution SAR polarimetric data," *J. Electron. Waves Appl.*, vol. 7, no. 5, pp. 717–737, 1993.

[22] R. Touzi and A. Lopes, "The principle of speckle filtering in polarimetric SAR imagery," *IEEE Trans. Geosci. Remote Sens.*, vol. 32, no. 5, pp. 1110–1114, Sep. 1994.

[23] J. S. Lee, M. R. Grunes, D. L. Schuler, E. Pottier, and L. Ferro-Famil, "Scattering-model-based speckle filtering of polarimetric SAR data," *IEEE Trans. Geosci. Remote Sens.*, vol. 44, no. 1, pp. 176–187, Jan. 2006.

[24] J. S. Lee, T. L. Ainsworth, Y. Wang, and K. S. Chen, "Polarimetric SAR speckle filtering and the extended sigma filter," *IEEE Trans. Geosci. Remote Sens.*, vol. 53, no. 3, pp. 1150–1160, Mar. 2015.

[25] Y. Wang, J. Yang, and J. Li, "Similarity-intensity joint PolSAR speckle filtering," in *Proc. Int. Conf. Radar*, 2016, pp. 1–5.

[26] F. Lang, J. Yang, and D. Li, "Adaptive-window polarimetric SAR image speckle filtering based on a homogeneity measurement," *IEEE Trans. Geosci. Remote Sens.*, vol. 53, no. 10, pp. 5435–5446, Oct. 2015.

[27] M. Yahia and T. Aguili, "Characterization and correction of multilook effects on eigendecomposition parameters in PolSAR images," *IEEE Trans. Geosci. Remote Sens.*, vol. 53, no. 9, pp. 5237–5246, Sep. 2015.

[28] M. Yahia, T. Hamrouni, and R. Abdelfatah, "Infinite number of looks prediction in SAR filtering by linear regression," *IEEE Geosci. Remote Sens. Lett.*, vol. 14, no. 12, pp. 2205–2209, Dec. 2017.

[29] M. Yahia, T. Ali, M. M. Mortula, R. Abdelfattah, and S. El Mahdi, "Infinite number of looks prediction in PolSAR filtering by linear regression," in *Proc. Int. Geosci. Remote Sens. Symp.*, 2020, pp. 1327–1330.

[30] S. V. Vaseghi, *Advanced Digital Signal Processing and Noise Reduction*, 4th ed., Hoboken, NJ, USA: Wiley, Jan. 2009, pp. 227–254.

[31] T.B. A.Lapini, F. Argenti, and L. Alparone, "Blind speckle decorrelation for SAR image despeckling," *IEEE Trans. Geosci. Remote Sens.*, vol. 52, no. 2, pp. 1044–1058. Feb. 2014.

[32] R. Abergel, L. Denis, F. Tupin, S. Ladjal, C.-A. Deledalle, and A. Almansa, 'Resolution-preserving speckle reduction of SAR images: The benefits of speckle decorrelation and targets extraction," in *Proc. Int. Geosci. Remote Sens. Symp.*, 2017, pp. 608–611.

[33] A. Arienzo, F. Argenti, and L. Alparone, "Impact of a spatial decorrelation of the noise on the performance of despeckling filters for polarimetric SAR data," in *Proc. Photon. Electromagnetics Res. Symp.*, Jun. 2019, pp. 1113–1121.

[34] X. Ma, P. Wu, Y. Wu, and H. Shen, "A review on recent developments in fully polarimetric SAR image despeckling," *IEEE J. Sel. Top. Appl. Earth Observ. Remote Sens.*, vol. 11, no. 3, pp. 743–758, Mar. 2018.

[35] S. Cloude and E. Pottier, "A review of target decomposition theorems in radar polarimetry," *IEEE Trans. Geosci. Remote Sens.*, vol. 34, no. 2, pp. 498–518, Mar. 1996.

[36] J. S. Lee, T. Ainsworth, J. Kelly, and C. López–Martínez, "Evaluation and bias removal of multi-look effect on entropy/alpha/anisotropy in polarimetric SAR decomposition," *IEEE Trans. Geosci. Remote Sens.*, vol. 46, no. 10, pp. 3039–3052, Oct. 2008.

[37] H. Feng, B. Hou, and M. Gong, "SAR image despeckling based on local homogeneous-region segmentation by using pixel-relativity measurement," *IEEE Trans. Geosci. Remote Sens.*, vol. 49, no. 7, pp. 2724–2737, Jul. 2011.

[38] [Online]. Available: https://earth.esa.int/web/polsarpro/home

Mohamed Yahia received the B.Sc. degree from Higher School of Sciences and Techniques, Tunis, Tunisia, in 2000, the M.Sc. degree from Higher School of Communication, Tunis, Tunisia, in 2002, the Ph.D. degree in telecommunication engineering conjointly from the National Engineering School of Gabes, Zrig Eddakhlania, Tunisia, and the Ecole Nationale Supérieure d'Electrotechnique, d'Electronique, d'Informatique, d'Hydraulique et des Télécommunications, Toulouse, France, in 2010, and the Habilitation degree in Telecommunications from University of Gabes, Zrig Eddakhlania, Tunisia, in 2017.

Since 2018, he has been an Associate Professor with NESG. In 2019, he is currently a Research Assistant at the American University of Sharjah, Sharjah, United Arab Emirates. His current research interests include analysis of polarimetric SAR images and numerical methods in electromagnetism.

Tarig Ali (Senior Member, IEEE) received the B.S. (Hons.) degree from University of Khartoum, Khartoum, Sudan, 1993, the M.S. and Ph.D. degrees from Ohio State University, Columbus, OH, USA, 1999, and 2003, respectively.

He is currently a Professor with the American University of Sharjah, Sharjah, United Arab Emirates. His research interests include GIScience, LiDAR mapping, mobile and Internet-based GIS, coastal mapping & GIS, applications of GIS/remote sensing in environmental and transportation engineering, wide-area GPS networks, and infrastructure monitoring/surveillance.

Md. Maruf Mortula received the B.Sc. degree from Bangladesh University of Engineering and Technology, Dhaka, Bangladesh, 2000, the M.Sc. and Ph.D. degrees from Dalhousie University, Halifax, NS, Canada, 2002 and 2006.

Since 2019, he has been a full Professor at the American University of Sharjah, Sharjah, United Arab Emirates. His research interests include water and wastewater treatment, recycling of solid waste management, water quality management in coastal water, and water infrastructure management.

Riadh Abdelfattah (Senior Member, IEEE) received the Engineer degree from the Telecommunication Engineering School of Tunis, Tunis, Tunisia, in 1995, the Master Degree (DEA) and the Ph.D. degree in electrical engineering from the "Ecole NationaleIngénieurs de Tunis," Tunis, Tunisia, in 1995 and 2000 respectively, and "le Diplôme de l'HabilitationUniversitaire" from SUP'COM from the University of Carthage in Tunisia, Carthage, Tunisia, in 2008.

Since December 15, 2017, he has been the Vice President with the University of Carthage and a Professor with the Higher School of Communications for engineers (SUP'COM), University of Carthage. He also is currently an Associate Researcher with the Department ITI, IMT-Atlantique, Brest, France. Between 2000 and 2002 he was a Postdoctoral Researcher at the EcoleNationale des Télécommunications, Paris, France, consecutively with the Department TSI and then with the Department of COMELEC. His main research interests include interferometric radar imagining, multiemporal and multiscale image analysis, desertification, flooding and soil salinity mapping from remote sensed data, and SAR-nanosatellite development.

Dr. Abdelfattah is a member of the Executive Committee of the IEEE Tunisia Section (2013–2015). He is an elected member at the scientific council of the Agence Universitaire de la Francophonie (2016–2018) and a member of the "Commission Régionale des Experts" of AUF. He was an elected member (2011–2017) with the University Council of Carthage. He is co-chairing the M2GARSS (Mediteranean and MENA Geoscience and Remote Sensing Symposium) symposium to be held in Tunis in March 2020. He is a founding member of the Research Unit in Satellite Imagery and its Applications (2004–2011), and a founding member of the Communication, Signal and Image Laboratory in November 2011 at SUP'COM. He has authored and co-authored more than 70 journal papers, conference papers and book chapters.

Samy Elmahdy received the B.Sc. degree in geology from Ain Shams University, Cairo, Egypt, and the M.Sc. degree in remote sensing, and the Ph.D. degree in the application of GIS and geomatics engineering in geotechnical engineering from the University of Putra, Selangor, Malaysia.

He has more than 25 years of experience in research with particular interest in quantitative remote sensing, GIS and geosciences. He has successfully published more than 35 research articles in journals and conference proceedings. He is currently a Geospatial Scientist with American University of Sharjah, Sharjah, United Arab Emirates.

Dr. Elmahdy was the recipient of the Gold Medal from the Malaysian National Space Agency in 2011 and won first place in the Rashid bin Humaid Award for Scientific Research in 2017.